



Contents lists available at ScienceDirect

Mechanism and Machine Theory

journal homepage: www.elsevier.com/locate/mechmt



Research paper

Design of a new foot structure based on the mast-type octahedral tensegrity structure



Jianwei Sun^{a,*}, Songyu Zhang^a, Zhenyu Wang^a, Guangsheng Song^b, Meiling Zhang^a, Jinkui Chu^c

^a School of Mechatronic Engineering, Changchun University of Technology, Changchun 130012, P. R. China

^b Key Laboratory of Bionic Engineering, Ministry of Education, Jilin University, Changchun, 130022, P. R. China

^c School of Mechanical Engineering, Dalian University of Technology, Dalian 116023, P. R. China

ARTICLE INFO

Keywords:

Tensegrity structure
Locking mechanism
Adaptive motion
Foot structure
Mast-type octahedral structure

ABSTRACT

Foot performance plays an important role in the walking-style robot walking in complex ground. This paper proposes a new foot structure based on the mast-type octahedral tensegrity structure with the flexibility, self-stability and self-adaptability. First, the mast-type octahedral tensegrity structure is evolved, and the feasibility of the motion is verified by dynamic analysis, and the degrees of freedom of the structure are limited by adding cross-axis. Next, by adding a locking structure based on a ratchet structure, and it avoided the structural instability caused by excessive deformation of the tensegrity foot structure. Finally, the design of the new foot structure was completed and a physical prototype was fabricated to verify the function of the new foot structure through relevant experiments. The high symmetry of the mast-type octahedral tensegrity structure simplifies the stiffness matching of the elastic members of the tension foot mechanism. The locking structure based on the ratchet structure is used to realize the switching of the flexible adaptation function and the rigid support function of the tensegrity foot structure, thus avoiding the structural instability caused by excessive deformation of the tensegrity foot structure.

1. Introduction

The foot, a part of the human in direct contact with the ground during walking, has evolved in nature to develop the ability to adaptively walk on complex ground and plays a vital role in the gait walking process. Similarly, the motion of the foot is closely related to vibration damping and load-bearing stability. For robots, the foot structure also plays a crucial role. Currently existing foot structures can be divided into two categories: passive foot structures and powered foot structures.

Most traditional foot structures are passive foot structures. At first, the traditional foot structure generally has the characteristics of a single structure and poor flexibility. For example, the most common traditional foot structure is the SACH foot [1]. Although the rigid wood keel in the structure provides neutral stability, this construction can seldom move laterally and is also the simplest type of jointless foot structure. The dynamic response ankle foot or energy storage and return (ESR) foot [2] is based on a stiff carbon fiber board. During the gait cycle, the center of mass of the foot structure can assist in the forward transition through energy storage and release. Kim et al. [3] proposed a new method that dynamic locomotion could be achieved on unsupported passive-ankle biped robots by the whole-body locomotion controller (WBLC). Haohua Xiu et al. [4] presented a passive compliant ankle-foot prosthesis (CPAF)

* Corresponding author.

E-mail address: avensun@tom.com (J. Sun).

capable of 2-DOF rotation during locomotion.

With the gradual improvement of the foot structure-function, based on the traditional foot structure, some elastomers are added to simulate the muscles, ligaments, and arch of the human foot biological model, and some mechanical structures are added to improve the foot structure movement function. For example, Shepherd et al. [5] developed a passive ankle-foot prosthesis structure with customizable torque and angle profiles to rapidly adjust ankle stiffness, which can improve gait biomechanics during walking and many other mobility tasks. Nickel et al. [6] designed an ankle-foot prosthesis system using a cam clutch engagement and disengagement structure, and this foot prosthesis system can passively adapt to the ground slope during walking. The results of late standing experiments in plantar flexion showed the potential to store and release more energy than standard lower limb prostheses. Realmuto et al. [7] designed a prosthesis with a passive nonlinear spring, which requires significantly fewer active components than a linear spring.

The current stage of passive foot structure design can be divided into two directions, i.e., the pursuit of a high degree of adaptive flexible foot and the pursuit of stable support of the rigid foot. The former uses flexible members to replace some of the rigid structures in the system to achieve self-adaptability to complex road surfaces by increasing degrees of freedom, but loses structural stability under high loads and is therefore prone to overturning. In contrast, the latter is mostly assembled with high stiffness and high precision mechanical parts, whose superior rigidity can carry robots with greater dead weight. However, robots equipped with this type of foot structure usually rely on a large number of sensors and control programs to achieve posture stability on rough terrain, which undoubtedly reduces the robot's fault tolerance and adds significant cost. Therefore, a foot structure with both adaptive and load-locking capabilities is particularly important in the current robot development trend.

Powered foot structures add some active drive devices such as pneumatic drives and electric drives in the foot structures, and some foot structures also add ankle joints, which can achieve multiple degrees of freedom of movement. Various actuators have been developed based on the existing foot-type mechanisms, such as, pneumatic or electric model. These actuators are used in foot and ankle prostheses, foot and ankle orthoses, foot and ankle exoskeletons and other devices to effectively assist patients in restoring kinematic behaviors and improving their biomechanical properties [8–11]. Zhanibek Issabekov [12] proposed an automated control scheme for manipulators controlling immobilized human limbs; Frank et al. [13] reported the design of a transferal pneumatic prosthesis. The Massachusetts Institute of Technology (MIT) Media Lab has conducted major research work on prosthetic feet with electric actuators. Hugh Herr et al. [14,15] developed a powered bionic foot-like structure that can be controlled to mimic normal human walking, and their team built several powered ankle-foot prosthetic robots, such as PowerFoot One, Rheo and Empower. Cherelle et al. [16] proposed a new energy-efficient dynamic ankle joint simulation prosthesis structure. Feng et al. [17] proposed a powered prosthesis with damping properties that can be adapted to different terrains; Dong et al. [18] proposed a new mechanical design for a motorized ankle prosthesis based on a geared five-rod spring mechanism. Lenzi et al. [19] developed a semiactive ankle prosthesis that utilizes a nonreverse driven cam follower mechanism that reduces the load on the moving parts and is longitudinally aligned with the foot when necessary to reduce the weight and size of the prosthesis. Most powered foot structures are designed with battery-operated servo motors and control systems; thus, powered foot structures are more complex and heavier than passive foot structures. However, the deficiencies of the passive foot structures such as complex mechanical structures, heavy masses and poor flexibility, are also problems that need to be solved. Therefore, there is still an urgent need to develop a new foot structure with a simple structure, light overall mass, flexibility, stability and self-adaptability under the condition of human ankle joint movement law.

The combination of robots and tensegrity structures has received increasing attention in recent years due to the advantages of both rigid and flexible structures. Intensity monolithic structures are widely used to optimize human joints because rigid structures can match bones, and flexible structures can match ligaments and muscle tissues [20]. Friesen et al. [21] proposed an underdriven lightly tensioned robot-assisted spine (hyperspine), and the ULTRA spine was further integrated into the quadruped robot Laika to better understand how vertebrates coordinate leg movements with a compliant spine. Rieffel and Mouret [22] describes an easy-to-assemble tensegrity-based soft robot capable of highly dynamic locomotive gaits and demonstrating structural and behavioral resilience in the face of physical damage. Mirletz et al. [23] developed a spine robot based on the mast type tensegrity spine structure, which can adapt to irregular terrain through a simple control system. Cui et al. [24] proposed a quadruped robot by combining the tensegrity structure with a rigid mechanism.

In the area of humanoid robots, Scarr [25] established a novel tensioned integral elbow joint. Li et al. [26] proposed a novel humanoid tensioned hand structure based on the reconfigurable properties of a tensegrity structure, which verified the self-stability and expandability of the grasping process. Baltaxe-Admony et al. [27] proposed a flexible bionic tensegrity shoulder joint robotic arm, which is more flexible than a conventional purely rigid robotic arm. Sun et al. [28] constructed a tensegrity wrist joint that can be stabilized using adaptive motion characteristics. Jung et al. [29] proposed a tensegrity structure-based lower extremity prototype which emulates the musculoskeletal connections of human lower extremity. Lee et al. [30] designed a proposed wrist is based on the concept of tensegrity structure which is similar to ligamentous structure combined with bones and ligaments so that it has compliant and lightweight properties. It is observed that the application of tensegrity structures in mechanical structure design can improve the flexibility of mechanical structures and then make the original structure function better.

For the study of the foot mechanism based on a tensegrity structure, Sun et al [31] proposed an adaptive bioinspired foot mechanism based on tensegrity structures and confirmed that the mechanism had good stability in an unstructured environment. With this adaptive bionic foot structure, in subsequent research work, the structural asymmetry leads to a complex stiffness matching process for the elastic members and can cause the bionic foot structure to collapse under excessive external loads due to the instability of the tensegrity structure. In this study, the mast-type octahedral tensegrity structure is evolved to give the equivalent structure of the mast-type octahedral tensegrity structure that can meet the functional requirements of the foot structure, and the high symmetry of the structure is used to realize the simplification of the stiffness matching of the elastic members of the tensegrity foot structure. The

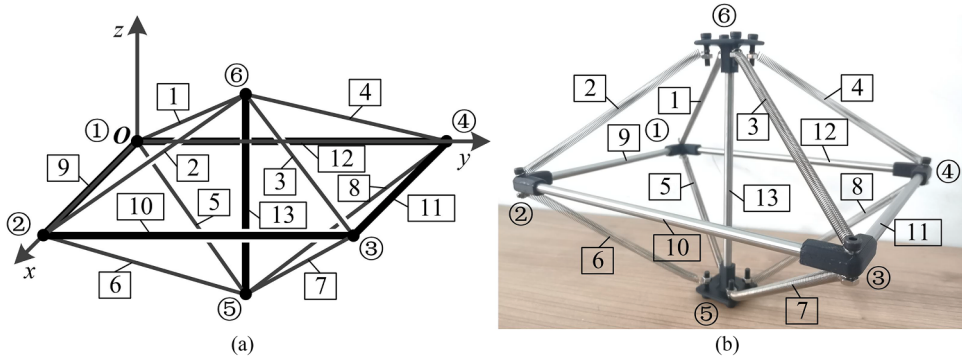


Fig. 1. MOTS schematic diagram: (a) Structure schematic diagram; (b) Physical model diagram.

degrees of freedom of the foot structure are limited by adding cross-axis. The locking structure based on the ratchet structure is used to realize the switching of the flexible adaptation function and the rigid support function of the tensegrity foot structure, thus avoiding the structural instability caused by excessive deformation of the tensegrity foot structure. Finally, the design of the new foot structure was completed and a physical prototype was fabricated to verify the function of the new foot structure through relevant experiments.

Based on the abovementioned research ideas, the chapters of this paper are organized as follows. In [Section 1](#), the current status of traditional and modern foot structures is outlined, and the advantages of tensegrity structures in optimizing human joints and the problems of previously designed foot structures are described. The remainder of this paper is organized as follows. In [Section 2](#), a structural description of the mast-type octahedral tensegrity structure is made, a mathematical model is established, and a simulation analysis of the dynamic process is performed by ADAMS. In [Section 3](#), the mechanical design of the foot structure is detailed. The mechanism mapping model is constructed, and a workspace analysis is performed based on the mechanism model diagram of the equivalent structure of the mast-type octahedral tensegrity structure. A locking structure based on the ratchet gear mechanism is designed to improve the stability of the foot structure. [Section 4](#) verifies the stability and adaptability of the foot structure, and the effectiveness of the locking structure using a physical prototype model. The conclusions are drawn in [Section 5](#).

2. Modeling

2.1. Description of the mechanism

The mast-type octahedral tensegrity structure (MOTS) is shown in [Fig. 1\(a\)](#). The structure is composed of 6 nodes and 13 members, where members 1, 2, 3, 4, 5, 6, 7 and 8 are cables and members 9, 10, 11, 12 and 13 are bars. Bars 9, 10, 11 and 12 form a rectangular frame.

With node 1 as the origin of the coordinate system, a Cartesian coordinate system is established with the x -axis coinciding with member 9, the positive direction of the x -axis pointing to node 2, the y -axis coinciding with member 12 and the positive direction of the y -axis pointing to node 4. The z -axis direction is determined according to the x -axis and y -axis. The position vectors of node i ($i = 1, 2, 3, 4, 5, 6$) are denoted as \mathbf{n}_i , and the spatial vector \mathbf{m}_i of the components can be expressed as

$$\begin{aligned} M &= [m_1 \ m_2 \ m_3 \ m_4 \ m_5 \ m_6 \ m_7 \ m_8 \ m_9 \ m_{10} \ m_{11} \ m_{12} \ m_{13}]^T \\ &= [n_1 - n_6 \ n_2 - n_6 \ n_3 - n_6 \ n_4 - n_6 \ n_1 - n_5 \ n_2 - n_5 \ n_3 - n_5 \ n_4 - n_5 \ n_2 - n_1 \ n_3 - n_2 \ n_4 - n_3 \ n_1 - n_4 \ n_5 - n_6]^T \end{aligned} \quad (1)$$

Then, the length of each member can be expressed as

$$l_i = \sqrt{\mathbf{m}_i^T \mathbf{m}_i}, \quad (i = 1, 2, \dots, 13) \quad (2)$$

The MOTS is twofold symmetric, with the following geometrical relationships.

$$\begin{cases} l_1 = l_2 = l_3 = l_4 \\ l_5 = l_6 = l_7 = l_8 \\ l_9 = l_{11} \\ l_{10} = l_{12} \end{cases} \quad (3)$$

When the lengths of the four cables above the rectangular frame are equal to the lengths of the four cables below, i.e., when the geometric relation of $l_i = l_j$ ($i = 1, 2, 3, 4; j = 5, 6, 7, 8$) is satisfied, the MOTS is threefold symmetric.

In the Cartesian coordinate system, the i -th member of the tensegrity structure can be described by the six generalized coordinates $[x_i \ y_i \ z_i \ \alpha_i \ \beta_i \ \gamma_i]$ to determine its position in space, as denoted by $\mathbf{q} = [x_i \ y_i \ z_i \ \alpha_i \ \beta_i \ \gamma_i]$. As shown in [Fig. 2](#), if the coordinates of node A are (x_A, y_A, z_A) , and the coordinates of the other node B can be expressed through the spatial Euler angles as

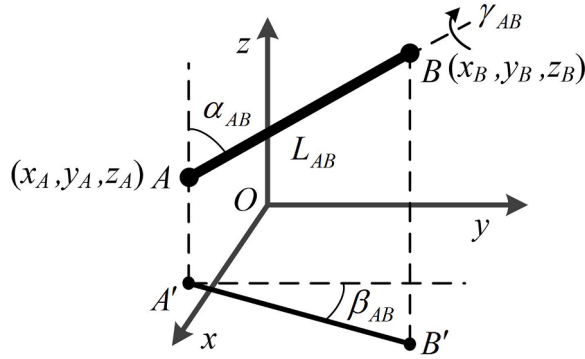


Fig. 2. The spatial position of bar AB in the Cartesian coordinate system.

$$B = \begin{bmatrix} x_A \\ y_A \\ z_A \end{bmatrix} + L_{AB} \cdot \begin{bmatrix} \sin\alpha_{AB}\sin\beta_{AB} \\ \sin\alpha_{AB}\cos\beta_{AB} \\ \cos\alpha_{AB} \end{bmatrix} \quad (4)$$

where L_{AB} is the distance from node A to node B. In the MOTS, the spatial relationship between node 5 and node 6 can be represented by the Euler angle α_{13} , β_{13} , γ_{13} of member 13 according to Eq. (2) as

$$n_6 = n_5 + l_{13} \cdot \begin{bmatrix} \sin\alpha_{13}\sin\beta_{13} \\ \sin\alpha_{13}\cos\beta_{13} \\ \cos\alpha_{13} \end{bmatrix} \quad (5)$$

where $n_5 = [x_5, y_5, z_5]^T$ and $n_6 = [x_6, y_6, z_6]^T$. All 8 cables are replaced with 8 identical lightweight springs, and the physical model is shown in Fig. 1(b). In the following analysis, the length of the spring is considered to vary according to Hooke's law. Since friction has a small effect on the results, it is ignored for the sake of convenience.

2.2. Inverse kinematic and static analysis

Skelton et al. [32,33] analyzed the statics/dynamics for a set of tensegrity structures in detail. These work provided the theoretical basis for our work. Static analysis is used to calculate the output variable of the structure φ if the structure is subjected to a specified external force and is in a state of hydrostatic equilibrium at the position of minimum total potential energy. Taking the spatial posture vector of member 13 $q = [x_5 \ y_5 \ z_5 \ \alpha_{13} \ \beta_{13} \ \gamma_{13}]$ as the generalized coordinates and establishing the energy equation of the mechanism, the elastic potential energy of the mechanism obtained by the MOTS after neglecting gravity can be expressed as

$$U(q) = \sum_{i=1}^8 \frac{1}{2} \cdot K_i \cdot (l_i - l_i^0)^2 \quad (6)$$

where K_i is the stiffness factor of the i -th spring, l_i^0 is the original length of the i -th spring, and l_i is the current length of the i -th spring. From the geometric constraint equations, it can be derived that

$$m_i \cdot m_i^T - l_i^2 = 0 \quad (7)$$

The output variable φ is used to denote the configuration of the MOTS, where

$$\varphi = \begin{bmatrix} n_5 \\ n_6 \end{bmatrix} \quad (8)$$

After considering the external forces, the overall potential energy of the body can be expressed as

$$\Pi(q) = U(q) - \int f^T \cdot dx_f \quad (9)$$

In the analysis, the rectangular frame is considered a fixed frame, and the lightweight rods and lightweight springs are considered to have negligible mass. $\int f^T \cdot dx_f$ is the work done by the external force f from the initial position φ_0 to the final position φ_n .

When the final external force is given, the external force applied to the MOTS gradually approaches the given value according to the mechanical properties of the spring. The external force f_i at the point of action can be linearized locally through Eq. (9).

$$\Pi_j = U_j - f_j^T \cdot \Delta x_{f_j} \quad (j = 1, 2, \dots, n) \quad (10)$$

where f is the external force applied on node 6. The structure enters the equilibrium position, and the position of the point of minimal

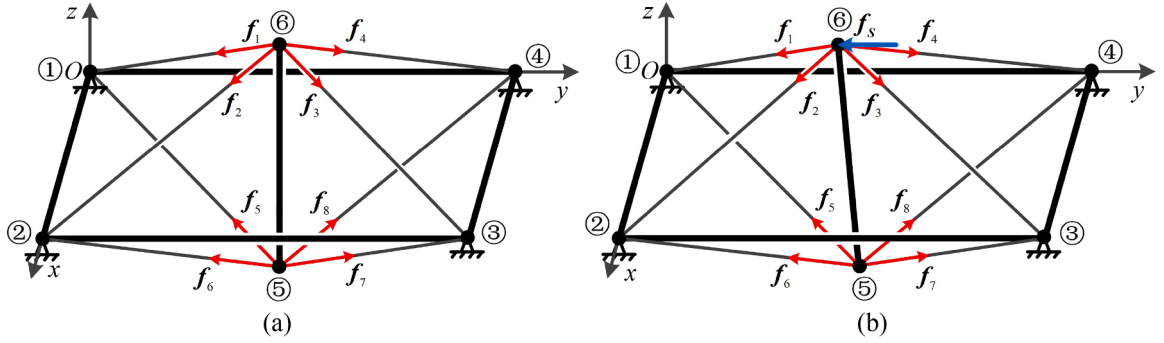


Fig. 3. Equilibrium states for different cases of the MOTS: (a) initial state of the MOTS; (b) static equilibrium state of the MOTS when subjected to an external load.

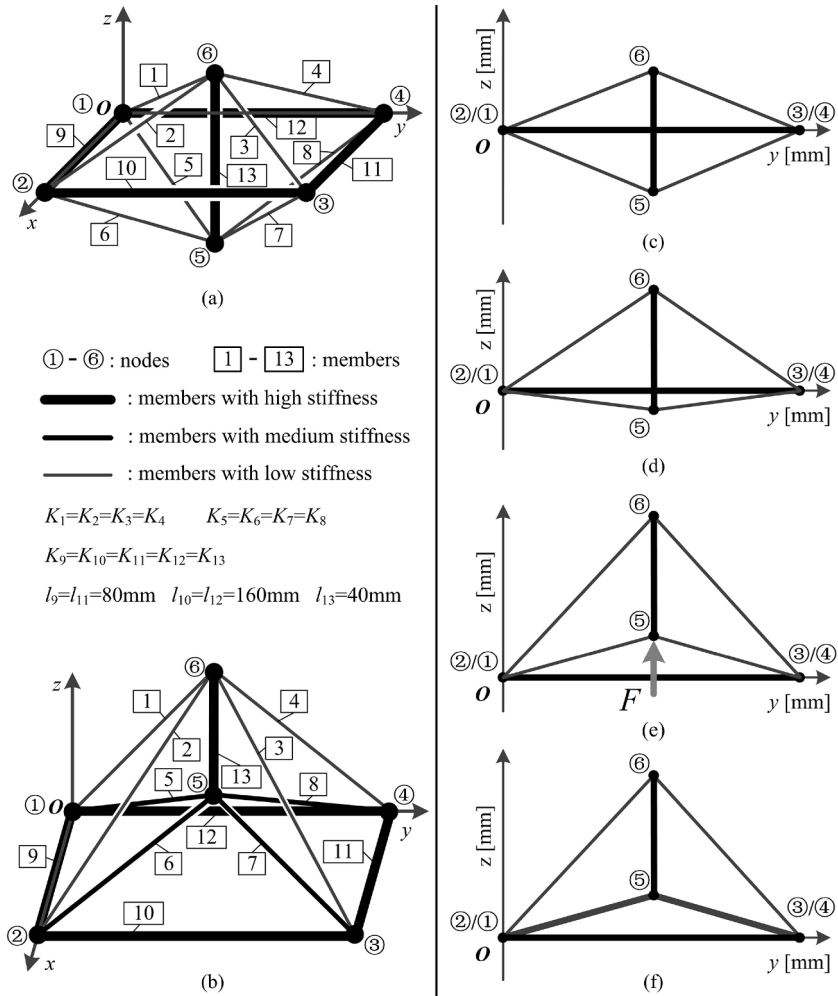


Fig. 4. Different structures of the MOTS: (a) Schematic diagram of the MOTS; (b) Schematic diagram of the eMOTS; (c) Projection view of the MOTS in the yOz plane; (d) Projection view of the MOTS with a change in elastic stiffness in the yOz plane; (e) Projection view of the MOTS under load conditions in the yOz plane; (f) Projection view of the MOTS equivalent structure in the yOz plane.

potential energy with known external forces and member lengths should satisfy the following conditions:

$$\frac{\partial \Pi(q)}{\partial q} = 0 \quad (11)$$

The MOTS is stabilized at the minimum potential energy when subjected to external forces; therefore, the final configuration is unique. We apply an external load f_S on the MOTS, in which the MOTS is in a stable state φ_S . The force applied to node 6 at this point is shown in Fig. 3(b), and the force equilibrium equation of the MOTS can be expressed as

$$\sum f = \sum_{i=1}^8 f_i + f_S = 0 \quad (12)$$

where $f_i = f_i \mathbf{r}_i$, $\mathbf{r}_i = \frac{\mathbf{m}_i}{|\mathbf{m}_i|}$ ($i=1, 2 \dots 8$) is the unit vector of the i -th member of the MOTS, f_i is the magnitude of the force on the i -th member and $f_i \geq 0$.

$$f_i = K_i \cdot (l_i - l_i^0) \quad (i=1, 2 \dots 8) \quad (13)$$

The external load on the configuration in each equilibrium state can be calculated by Eq. (12) through static analysis. The external load f_S on the MOTS when it is in configuration φ_S can be expressed as

$$f_S = - \sum_{i=1}^8 f_i \quad |f_i| \geq 0 \quad (14)$$

Without considering the self-weight of member 13, member 13 will be perpendicular to the plane in which the rectangular frame is positioned and will hang at the geometric center of the rectangular frame when the stiffness coefficients of all 8 lightweight springs are the same (as shown in Figs. 4(a) and 4(c)). When $K_j > K_i$ ($i=1, 2, 3, 4$; $j=5, 6, 7, 8$), the spatial position of member 13 will change, as shown in Figs. 4(d). As K_j ($j=5, 6, 7, 8$) approaches infinity, node 5 of member 13 gradually approaches or even overlaps the plane where the rectangular frame is located. Consider whether a vertical force F is applied at node 5 to suspend member 13 directly above the plane in which the rectangular frame is located (as shown in Fig. 4(e)). In this structural space position state, members 5, 6, 7 and 8 are replaced with compression members of lower axial stiffness, and the structure will reach a new equilibrium state through tensile and compression replacement (as shown in Fig. 4(f)). At this time, the structure is considered to be an equivalent structure of the mast-type octahedral tensegrity structure (eMOTS) (as shown in Fig. 4(b)).

2.3. Workspace analysis

According to the description method of the working space, the tensegrity structure can be divided into geometric workspace and equilibrium workspace. The geometric workspace can be analyzed according to three constraints, namely, the length constraint of the support chain, the corner constraint of the connection sub, and the interference constraint of the bar. When analyzing a balanced workspace, energy constraints are included in addition to the three conditional constraints of several workspaces. The energy constraint allows the mechanism to be balanced in the workspace. The specified reference point for the geometric workspace of the mechanism is the endpoint of the end-effector.

2.3.1. Branched chain length constraint

Since the length change of a lightweight spring under the action of an external force is finite, under the condition that Hooke's law is satisfied, each lightweight spring should satisfy the following conditions:

$$l_i^0 \leq l_i \leq l_{\max} \quad (15)$$

where l_{\max} is the maximum allowable length for a lightweight spring in MOTS.

2.3.2. Associate angle constraints

Each member of the MOTS is connected to the rectangular frame by spherical subarticulation. The limited angular range of the spherical subarticulation limits the motion of the mechanism; thus, the angular constraint at the hinge point of the member connection must be considered in the workspace of the mechanism.

$$\theta_i \leq \theta_{\max} \quad (16)$$

where θ_i is the rotation angle of the i -th spherical sub and θ_{\max} is the maximum allowable rotation angle of the i -th spherical sub.

2.3.3. Bar interference constraints

A finite bar size may cause interference. To simplify the study, the minimum distance between the member and each bar of the rectangular frame is calculated without considering the diameters of the constituent bars to determine whether the two bars interfere. The minimum distance d between bar 13 and each bar of the rectangular frame when the MOTS is subjected to external forces is

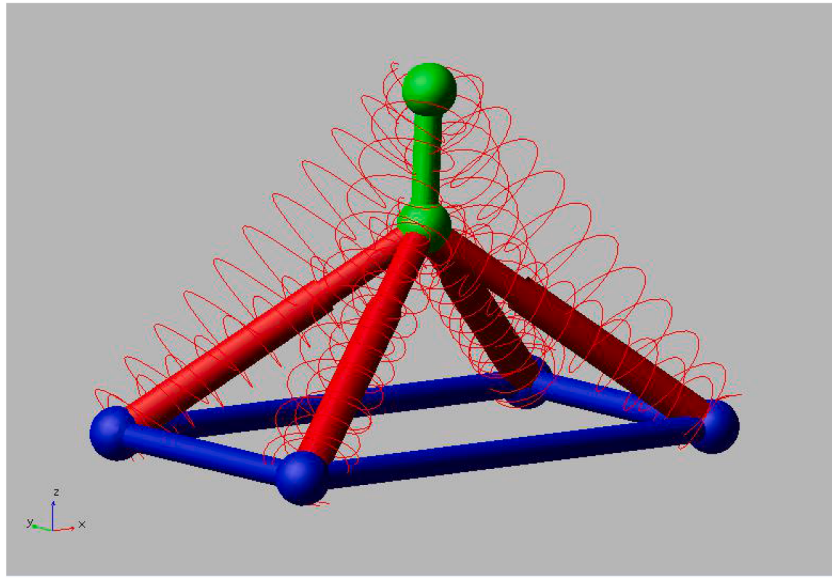


Fig. 5. The dynamic model of eMOTS implemented in ADAMS.

$$d = \min\left(\frac{|m_1 \cdot a_9|}{|a_9|}, \frac{|m_2 \cdot a_{10}|}{|a_{10}|}, \frac{|m_3 \cdot a_{11}|}{|a_{11}|}, \frac{|m_4 \cdot a_{12}|}{|a_{12}|}\right) \quad (17)$$

$$a_i = m_i \times m_{13} \quad (i = 9, 10, 11, 12) \quad (18)$$

2.3.4. Energy constraints

The number of variables that satisfy the energy constraint equation is determined according to the degrees of freedom of the overall tensioning mechanism. The energy constraint equation is expressed as follows:

$$\frac{\partial \Pi(q)}{\partial q} = 0 \quad (19)$$

where ψ is the positional variable that satisfies the energy constraint.

The constraint equations to be satisfied for the equilibrium workspace solution are as follows, i.e., the constraint equations that consist of Eqs. (15), (16), (17), and (19):

$$\begin{cases} l_i^0 \leq l_i \leq l_{\max} \\ \theta_i \leq \theta_{\max} \\ d \neq 0 \\ \frac{\partial \Pi(q)}{\partial q} = 0 \end{cases} \quad (20)$$

The fixed equilibrium attitude position workspace can be solved using a numerical method. First, given the range of values for each of the six positional variables in the feasible region, each set of positional variables is subjected to a series of relevant parameter calculations and substituted into the constraint equation for judgment. After judging all the positional variables in the feasible region, three positional variables for each group of positional variables in the geometric workspace are out. The three positional variables are the equilibrium reachable space.

In eq. (20), firstly, the geometrically reachable space of the component can be determined by length constraint, Angle constraint and interference constraint. After deformation by external forces, the eMOTS will exist in an equilibrium state in the geometrically reachable space. The elastic members of the eMOTS prefer configurations with smaller potential energy during deformation compared to other local minima with higher energy [34]. So the eMOTS will reach equilibrium at the minimum overall potential energy. $\Pi(q)$ represents the total potential energy of the body after deformation by external forces. $q = [x_5 \ y_5 \ z_5 \ \alpha_{13} \ \beta_{13} \ \gamma_{13}]$ represents the spatial posture vector of member 13. The position of equilibrium is the position with the least potential energy in the geometrically reachable space.

Table 1

The values of relevant parameters chosen for the eMOTS in this paper.

Parameter	Symbol	Value
The initial lengths of the members 1, 2, 3 and 4	$l_1^0, l_2^0, l_3^0, l_4^0$	80 mm
The initial lengths of the members 5, 6, 7 and 8	$l_5^0, l_6^0, l_7^0, l_8^0$	130 mm
The length of the members 9 and 11	l_9, l_{11}	80 mm
The length of the members 10 and 12	l_{10}, l_{12}	160 mm
The length of the members 13	l_{13}	40 mm
The stiffness of the members 1, 2, 3 and 4	K_1, K_2, K_3, K_4	0.3 N/mm
The stiffness of the members 5, 6, 7 and 8	K_5, K_6, K_7, K_8	0.5 N/mm

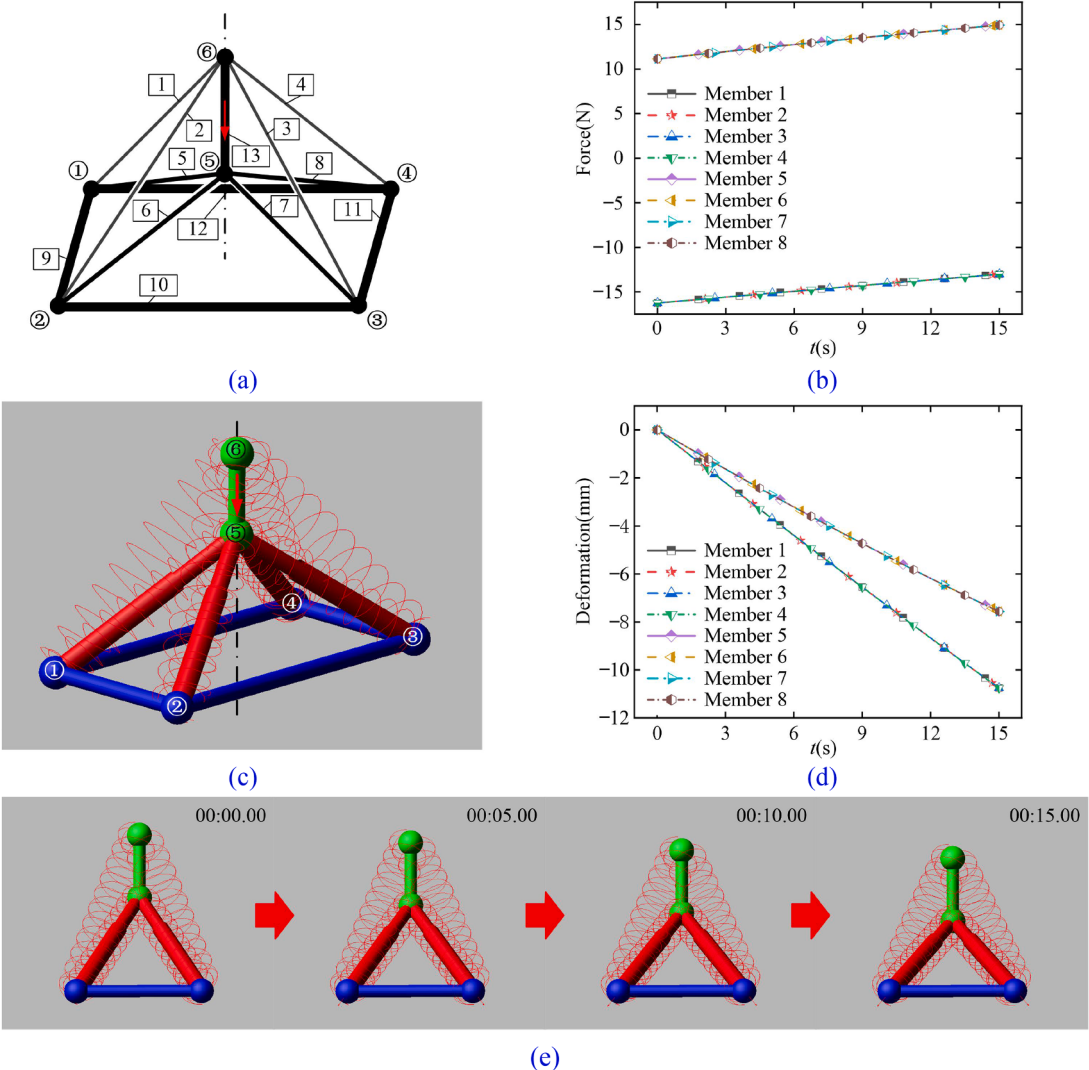


Fig. 6. Dynamic analysis of the uniform linear motion of member 13 in the eMOTS along the vertical direction downward: (a) Schematic sketch of the motion of the eMOTS; (b) Variation in the internal stress of the elastic member; (c) Schematic diagram of the dynamic model motion of the eMOTS; (d) Variation in the deformation variables of the elastic member; (e) Dynamic model motion process of the eMOTS.

2.4. Postural analysis

In this subsection, the dynamic process of the rigid member is solved using ADAMS to observe the variation of the elastic member. The rectangular frame and member 13 of the eMOTS are considered rigid bodies and implemented in ADAMS, as shown in Fig. 5. When the dimensions of the rigid members are determined, the initial lengths and stiffness coefficients of the elastic members are determined after testing in ADAMS to ensure a stable configuration of the eMOTS. In the dynamic analysis process of eMOTS, this eMOTS model is

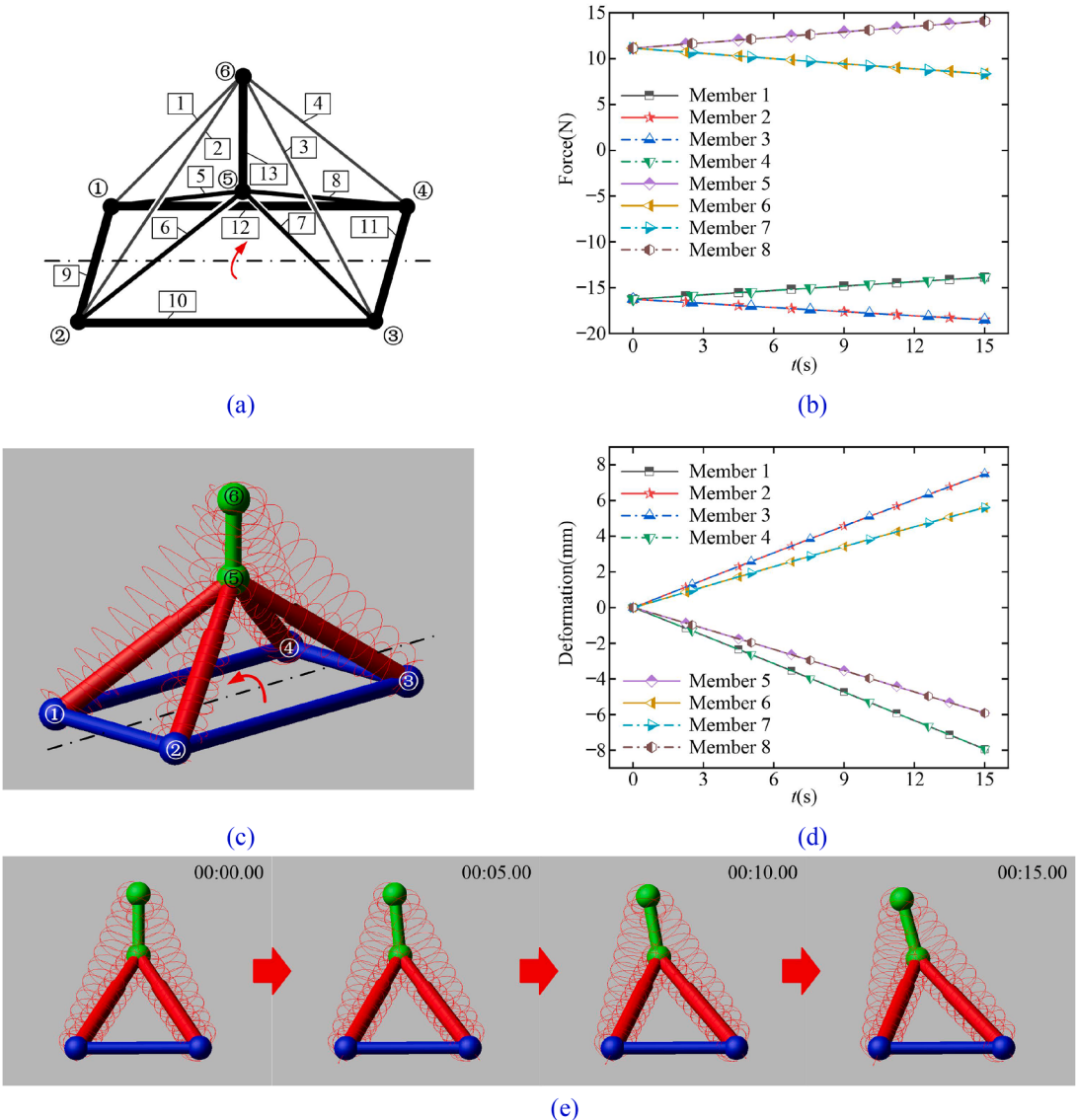


Fig. 7. Dynamic analysis of the rotation of member 13 around the midline of the short side of the rectangular frame in the eMOTS: (a) Schematic sketch of the motion of the eMOTS; (b) Variation in the internal stress of the elastic member; (c) Schematic diagram of the dynamic model motion of the eMOTS; (d) Variation in the deformation variables of the elastic member; (e) Dynamic model motion process of the eMOTS.

established based on the geometrical parameters of Table 1. Assuming that the rectangular frame is a fixed frame, we analyze the force and the amount of length change of each elastic member when the movement of member 13 occurs by the load.

When member 13 is loaded and moves downward with a uniform linear motion of 15 mm along the vertical direction at a speed of 1 mm/s, a schematic sketch of eMOTS motion is shown in Fig. 6(a). The elastic member will deform under the load force. The change in internal stress of the elastic member of the eMOTS is shown in Fig. 6(b); The eMOTS changes in the deformation of the elastic member are shown in Fig. 6(d), and the dynamic model motion process in ADAMS is shown in Fig. 6(e). When member 13 is loaded and moves 15° by rotation at a speed of 1°/s in the direction of the short side of the rectangular frame, a schematic sketch of the eMOTS motion, as shown in Fig. 7(a). The elastic member is deformed under the load force. The change in internal stress of the elastic member of the eMOTS is shown in Fig. 7(b); the change in deformation of the elastic member of the eMOTS is shown in Fig. 7(d), and the dynamic model motion process in ADAMS is shown in Fig. 7(e). When member 13 is subjected to load and moves 25° by rotation at 1°/s in the direction of the long side of the rectangular frame, the schematic sketch of eMOTS motion is shown in Fig. 8(a). The elastic member is deformed under the load force. eMOTS changes in the internal stress of the elastic member, as shown in Fig. 8(b). eMOTS changes in the deformation of the elastic member, as shown in Fig. 8(d), and the dynamic model motion process in ADAMS is shown in Fig. 8(e).

After the dynamic analysis of the eMOTS model in ADAMS and the observation of the deformation of the configuration of the eMOTS dynamic model, it can be seen that its rotational movements can simulate well the dorsiflexion, plantar flexion, inversion and

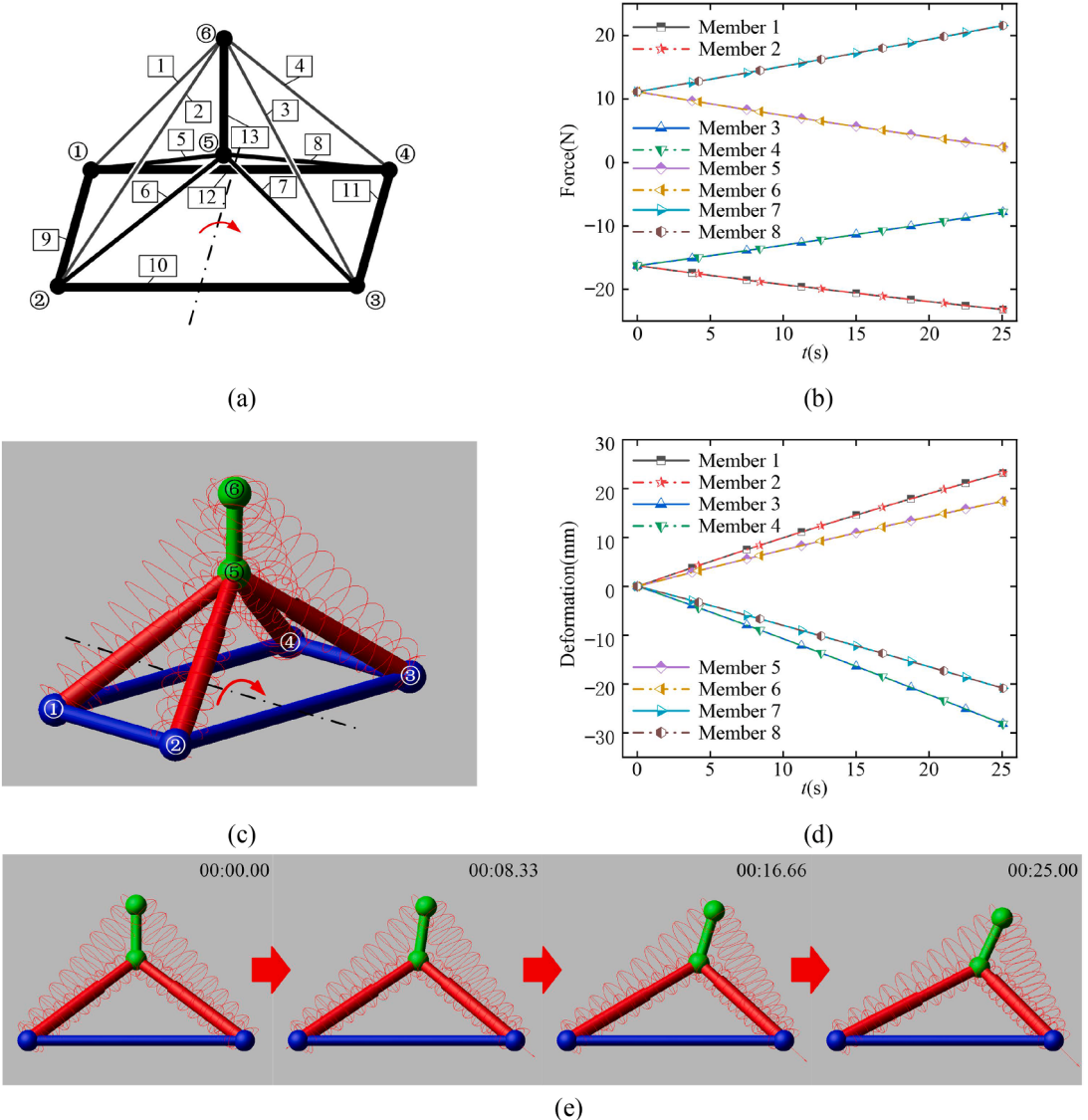


Fig. 8. Dynamic analysis of the rotation of member 13 around the midline of the long side of the rectangular frame in eMOTS: (a) Schematic sketch of the motion of the eMOTS; (b) Variation in the internal stress of the elastic member; (c) Schematic diagram of the dynamic model motion of the eMOTS; (d) Variation in the deformation variables of the elastic member; (e) Dynamic model motion process of the eMOTS.

valgus movements of the ankle joint of the human foot structure. However, in addition to the abovementioned simulated actions, there are still multiple degrees of freedom in the eMOTS. To avoid the collapse of the structure when the eMOTS is subjected to an external load, we further improve the design of the eMOTS.

3. Design of new foot structure

3.1. Conformation design of new foot structure

3.1.1. Mechanistic mapping models

According to the tensegrity schematic of the eMOTS, as shown in Fig. 4(b), the overall structural model of the tensioning based on the eMOTS is established (Fig. 9(a)). Parts 1, 2, 3, 4 and 5 correspond to members 13, 5, 6, 7 and 8, respectively, in the tensegrity schematic. The red connectors correspond to members 1, 2, 3, and 4, and the arrows indicate the direction of tension transfer.

The equivalent structure of the MOTS is similar to the morphological structure of the human foot. Through the principle of similarity, elastic members are used to simulate the foot muscles and ligaments, and rigid members are used to simulate the foot bones. Based on the shock absorption characteristics of the human foot, an elastic structure with stretch characteristics can be used to replace

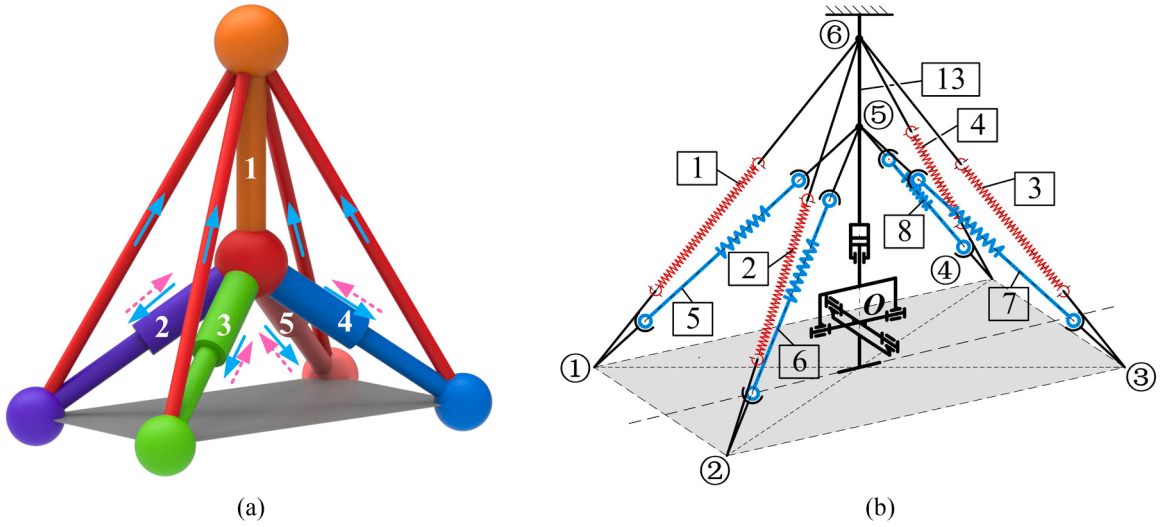


Fig. 9. eMOTS: (a) Tensegrity structural model diagram; (b) Mechanistic mapping model diagram

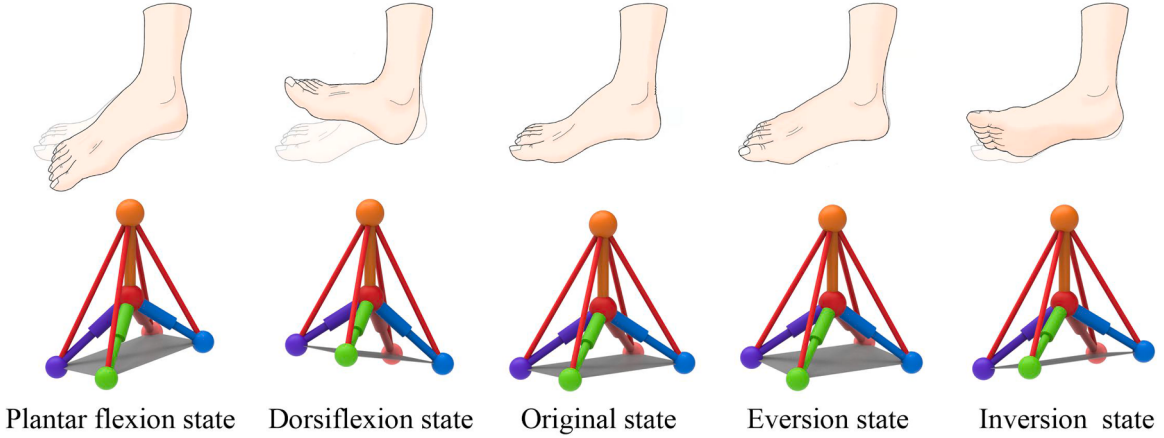


Fig. 10. Similar motion characteristics between the human foot and the tensegrity structural model.

parts 2, 3, 4 and 5 of the tensegrity structural model, a rigid thin plate can be used to replace the sole of the foot, and the theory and method of mechanism science can be combined to design a new foot structure. The new foot structure based the eMOTS is shown in Fig. 9(b) as a mechanistic mapping model by using a moving sub and a cross shaft to achieve motion of the new foot structure and an elastic structure with telescopic features whose ends are connected by a ball sub. Based on the ankle joint motion characteristics of the human foot, the cross-axis equivalent is used to simulate the motion characteristics of the ankle joint. The tensegrity structural model established based on the eMOTS can achieve motion characteristics similar to those of the human foot under the action of the cross-axis, as shown in Fig. 10.

3.1.2. Spatial analysis of the institutional mapping model

Obviously, the foot structure can only match the human foot motion if there is an overlap between the workspace of the tensegrity foot structure and the human foot motion range, so a workspace analysis of the structure is necessary. The mechanistic mapping model of the eMOTS is used to solve the position workspace of its geometric fixed attitude through numerical methods. Since the length change of a compression spring under the action of an external force is finite, under the condition that Hooke's law is satisfied, each compression spring should satisfy the following conditions:

$$l_{\min} \leq l_p \leq l_{\max} \quad (21)$$

where l_{\min} is the minimum allowable length of the p -th compression spring in eMOTS, and l_{\max} is the maximum allowable length of the p -th compression spring in eMOTS.

Eq. (21) as a constraint on the workspace of the mechanistic mapping model of eMOTS, a sketch of the institutional mapping model

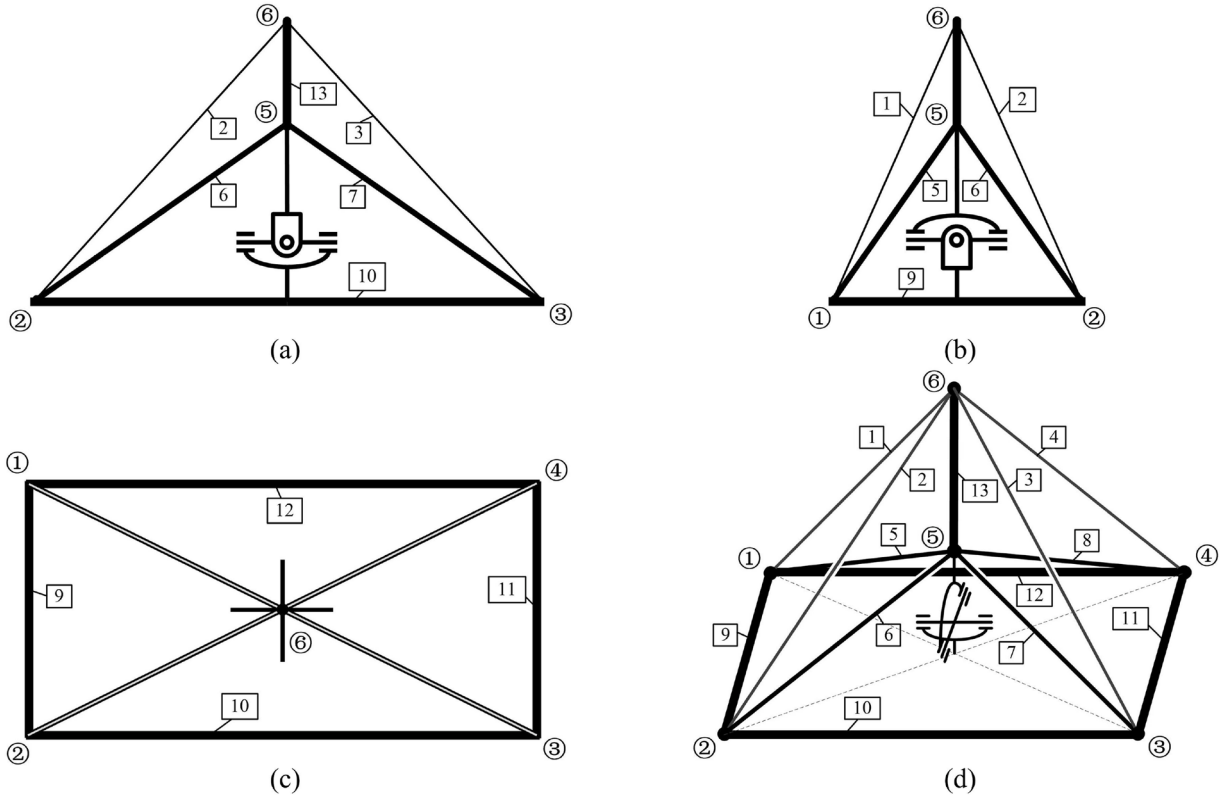


Fig. 11. Sketch of the mechanistic mapping model: (a)~(c) Three views of the mechanistic mapping model; (d) Three-dimensional view of the mechanistic mapping model.

based on the physiological structural parameters of the human foot is shown in Fig. 11, with the following institutional parameters. $l_1^0=l_2^0=l_3^0=l_4^0=80$ mm, $l_5^0=l_6^0=l_7^0=l_8^0=130$ mm, $l_9=l_{11}=160$ mm, $l_{10}=l_{12}=40$ mm, $l_{h1}=40$ mm, $l_{h2}=20$ mm, where the distance from node 6 to the center of the cross shaft pivot is l_{h1} and the distance from the center of the cross shaft pivot to the plane where the rectangular frame is located is l_{h2} .

With the center of rotation of the cross-axis as the origin, the x -axis is parallel to member 9, the positive direction is from node 1 to node 2, the y -axis is parallel to member 10, the positive direction is from node 2 to node 3, the z -axis is coincident with member 13, and the positive direction is from node 5 to node 6, as shown in Fig. 11. The step size of the loop variable is $\Delta\alpha = \Delta\beta = \pi/200$, $k_i \in [90, 120]$ ($i=5, 6, 7, 8$), $x \in [-40, 40]$, $y \in [-80, 80]$, $z \in [-20, 100]$, $\alpha \in [0, \pi/2]$, $\beta \in [-\pi, \pi]$, $\gamma \in 0$.

The balanced fixed posture position workspace is shown in Fig. 12(a). The cross-axis rotation center simulates the ankle joint of the human foot, rod 13 simulates the calf connected to the ankle joint, node 6 of member 13 simulates the top position of the calf, node 5 simulates the middle position of the calf, and the motion space of the lower leg that meets the requirements of human foot movement can reach the working space shown in Fig. 12(b) when the ankle joint is turned inward or outward by 15° and dorsiflexed or plantar flexed by 25°.

As shown in Fig. 12, the shape of the workspace is clearly observed, and the workspace is symmetric about the xOz plane and the yOz plane according to Fig. 12(d). The conforming motion space of the lower leg is within the range of the workspace of the balanced fixed posture position, and the MOTS mechanical mapping model can meet the human foot reachable space requirement in the motion space.

3.2. Locking mechanism

3.2.1. Structure and working principle

Two degrees of freedom of dorsiflexion or plantar flexion, inversion or valgus can be well realized by the cross-axis connection. The eMOTS has the flexibility of the tensegrity structure. To further improve the stability of the new foot structure based on the eMOTS, the foot structure can be switched between rigid and flexible at any angle. A locking mechanism is added on the basis of a ratchet gear structure for the eMOTS, which includes a pawl and two sets of bidirectional passively rotating ratchet gears. The structure principle is shown in Fig. 13.

Two sets of bidirectional passive rotary ratchet gear structures are placed vertically to control plantar flexion, dorsiflexion, inversion and valgus of the foot structure. The effect of the prototype is shown in Fig. 13(a). Each set of directional passive rotating

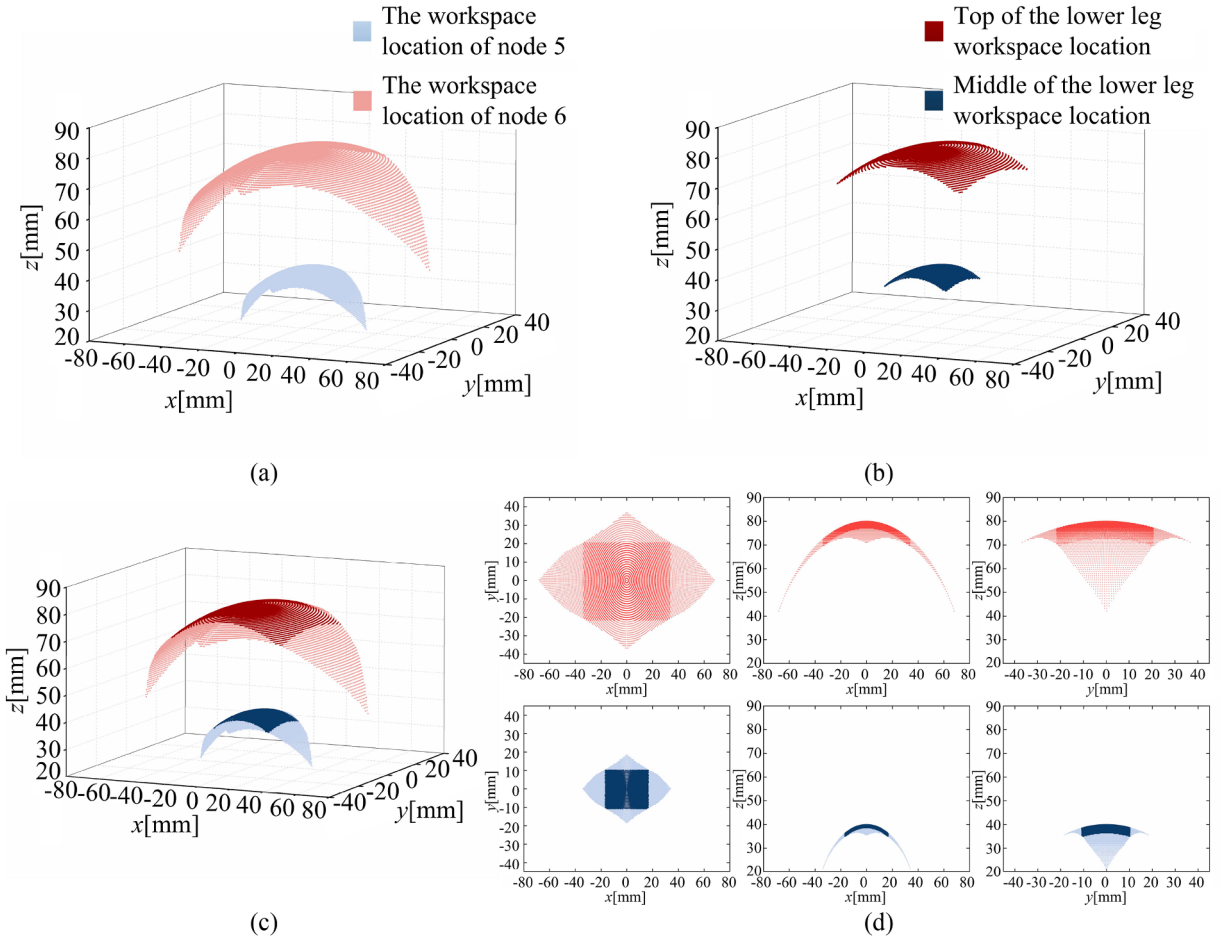


Fig. 12. Workspace: (a) The MOTS mechanism mapping model reachable workspace; (b) Motion space of the lower leg that meets the requirements of human foot movement that reach the working space; (c) Motion space of the lower leg that meets the requirements of human foot movement versus the working space in a balanced fixed posture position; (d) Two-dimensional projection view of the spatial contrast map.

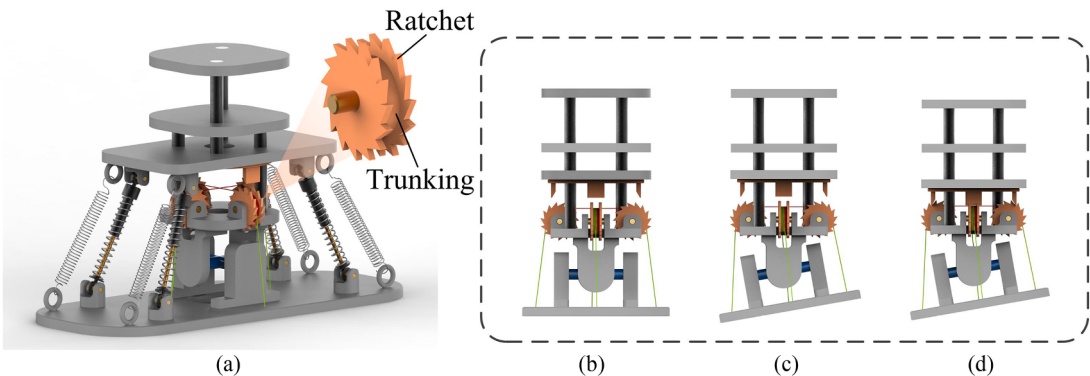


Fig. 13. Prototype effect: (a) Detailed drawing of the locking structure; (b) Locking structure in the initial state; (c) Locking mechanism in the motion state; (d) Locking structure in the locked state.

ratchet gear structures consists of two ratchet gears and three cables, which connect and link the two ratchet gears to the footplate through three cables and ensure that the two ratchet gears maintain the same angular speed around the center of rotation during motion. There is a certain angle when the foot structure travels on unstructured ground. According to the adaptive nature of the tensegrity structure, first the angle of the bottom plane will change, and by linkage, the ratchet will also produce an angle change, as

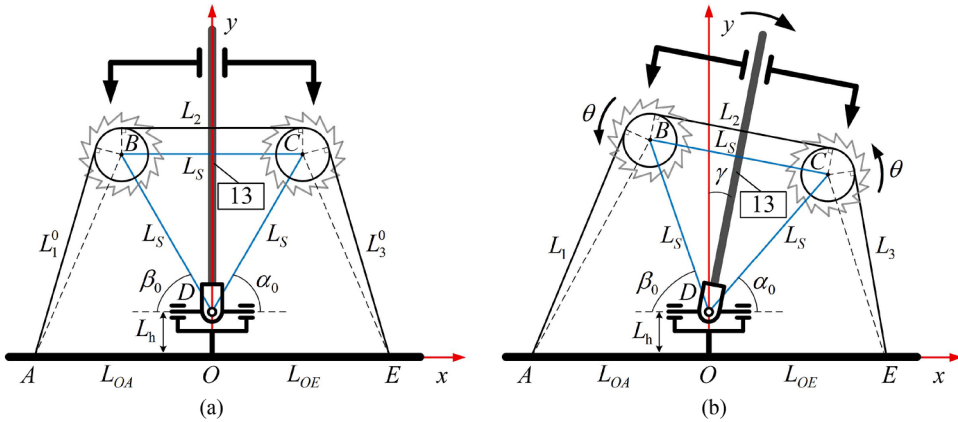


Fig. 14. Schematic diagram of the ratchet locking mechanism of the cable drive: (a) Schematic diagram of the ratchet locking mechanism in the initial state; (b) Schematic diagram of the ratchet locking mechanism in the motion state.

shown in Fig. 13(c). When the foot structure receives a load, the ratchet will lock, which transforms the foot structure from a flexible adaptive road surface to a rigid foot structure, as shown in Fig. 13(d). From the moment that the foot structure receives a reduced load until it disappears, the ratchet lock opens, and when the foot structure gradually leaves the road, the foot structure returns to its initial stable state according to the self-recovery property of the tensegrity structure, as shown in Fig. 13(b). The load on the foot structure can be achieved by the gravity of the robot during alternating bipedal walking.

3.2.2. Kinematic analysis of the ratchet locking structure

As shown in Fig. 14(a), node D is the center of rotation of the cross axis, the height of node D and the rectangular plane is L_h , and node A and node E are in the rectangular plane. The center of line AE is the origin O, the direction of OE is the positive direction of the x-axis, the direction of OD is the positive direction of the y-axis to establish a Cartesian coordinate system, and the lengths of lines OA and OE are denoted by L_{OA} and L_{OE} , respectively. Node B and node C are the centers of rotation for ratchet gear B and ratchet gear C, respectively, and the inner diameter of the ratchet gear is r . In the spatial position, triangle BCD enclosed by nodes B, C and D as the vertices is an equilateral triangle. The side length of equilateral triangle BCD is L_s . α_0 and β_0 denote the angle between side CD and side BD of equilateral triangle BCD and the horizontal direction of the x-axis, respectively. The relationship between the deflection angle γ (positive clockwise) when bar 13 is in relation to the bottom rectangular plane and the ratchet rotation angle θ (positive clockwise) can be explored through geometric constraints. Based on the given geometric parameters, the position vector of each node can be determined as follows:

$$A = [-L_{OA} 0]^T, B = [x_B y_B]^T, C = [x_C y_C]^T, D = [0 L_h]^T, D = [L_{OE} 0]^T \quad (22)$$

When the magnitude of the resulting deflection angle between bar 13 and the bottom rectangular plane is γ , the relationship between γ and α_0, β_0 , can be expressed as

$$g = 60^\circ - \alpha_0, g = b_0 - 60^\circ \quad (23)$$

According to the geometric relationship, the position vectors of node B and node C can be expressed as

$$B = \begin{bmatrix} x_B \\ y_B \end{bmatrix} = \begin{bmatrix} -L_s \cos \beta_0 \\ L_h + L_s \sin \beta_0 \end{bmatrix} \quad (24)$$

$$C = \begin{bmatrix} x_C \\ y_C \end{bmatrix} = \begin{bmatrix} L_s \cos \alpha_0 \\ L_h + L_s \sin \alpha_0 \end{bmatrix} \quad (25)$$

From Eq. (24) and (25), the lengths L_{AB} and L_{CE} of the line segments AB and CE can be obtained as

$$L_{AB} = |B - A| = \sqrt{(L_{OA} - L_s \cos \beta_0)^2 + (L_h + L_s \sin \beta_0)^2} \quad (26)$$

$$L_{CE} = |C - E| = \sqrt{(L_{OE} - L_s \cos \alpha_0)^2 + (L_h + L_s \sin \alpha_0)^2} \quad (27)$$

Then, the tangent lengths L_1 and L_3 from node A and node E to ratchet gear B and ratchet gear C are

$$L_1 = \sqrt{L_{AB}^2 - r^2} = \sqrt{(L_{OA} - L_s \cos \beta_0)^2 + (L_h + L_s \sin \beta_0)^2 - r^2} \quad (28)$$

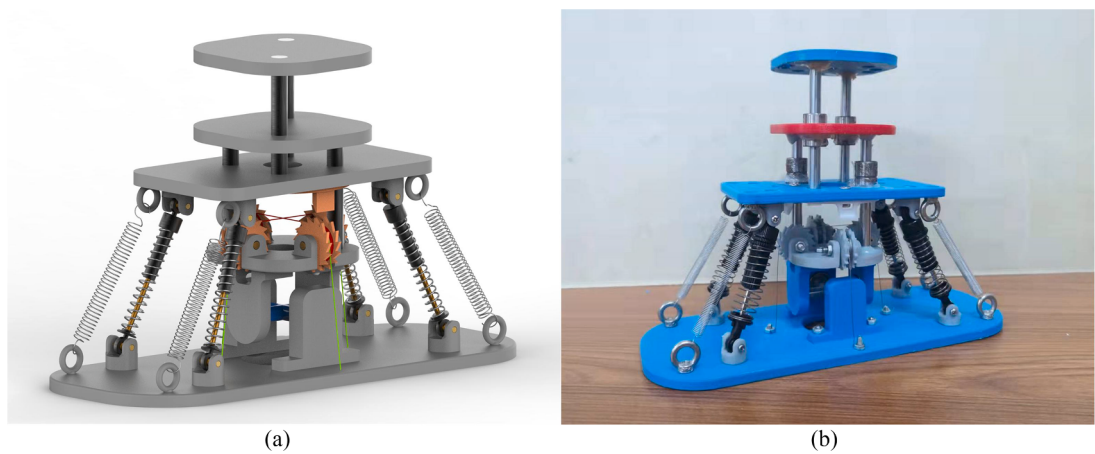


Fig. 15. New foot structure: (a) Physical prototype model; (b) Instantiated devices.

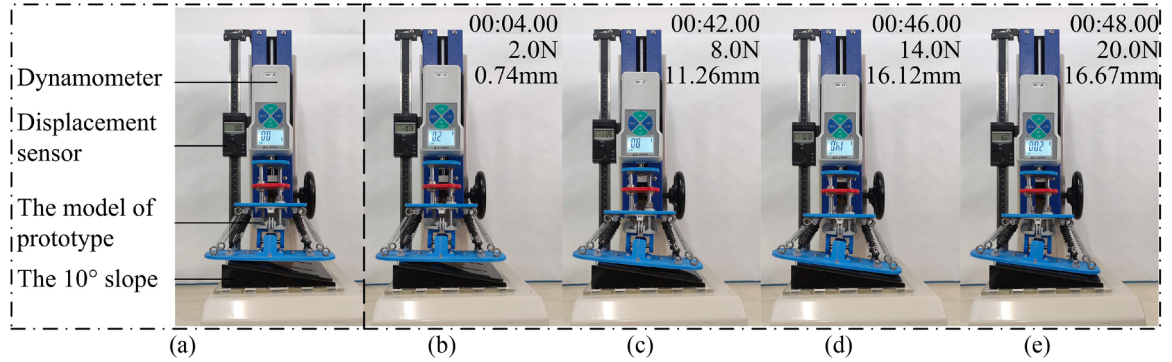


Fig. 16. Sloping foot structure subjected to load testing: (a) The experimental platform of stress testing; (b)~(e) The process of stress testing the prototype.

Table 2

Slope eversion and dorsiflexion displacement experimental data under the external load.

F/(N)	2	4	6	8	10	12	14	16	18	20
$x_1/(mm)$	1.22	3.58	8.31	10.03	11.19	11.59	11.91	12.00	12.12	12.24
$x_2/(mm)$	0.74	2.42	7.60	11.26	13.39	14.97	16.12	16.40	16.48	16.67
$x_3/(mm)$	0.39	2.49	4.27	5.52	8.60	9.80	10.05	10.33	10.42	10.57
$x_4/(mm)$	1.18	4.45	9.45	10.80	12.26	13.23	13.62	13.98	14.12	14.34

$$L_3 = \sqrt{L_{CE}^2 - r^2} = \sqrt{(L_{OE} - L_S \cos\alpha_0)^2 + (L_h + L_S \sin\alpha_0)^2 - r^2} \quad (29)$$

where the relationship between the deflection angle γ and angle α_0 and β_0 satisfies Eq. (23). In equilibrium ($\gamma = 0$), the lengths of the cords connected to nodes A and E are L_1^0 and L_3^0 , which can be expressed as

$$L_1^0 = L_3^0 = \sqrt{\left(L_{OA} - \frac{L_S}{2}\right)^2 + \left(\frac{\sqrt{3}}{2}L_S - L_h\right)^2} \quad (30)$$

The length of the cable that connects the two ratchets is L_2 , and $L_2 = L_S$ remains a constant during deflection. When bar 13 is deflected clockwise, as shown in Fig. 14(b), the ratchet will rotate counterclockwise with an angle of rotation of magnitude. The rotation angle θ can be obtained from the amount of change in the cable length ΔL_1 with connecting node A as follows: (When bar 13 is deflected counterclockwise, the ratchet will rotate clockwise, and the angle of rotation θ can be obtained from the amount of change in the cable length ΔL_1 with connection node E.)

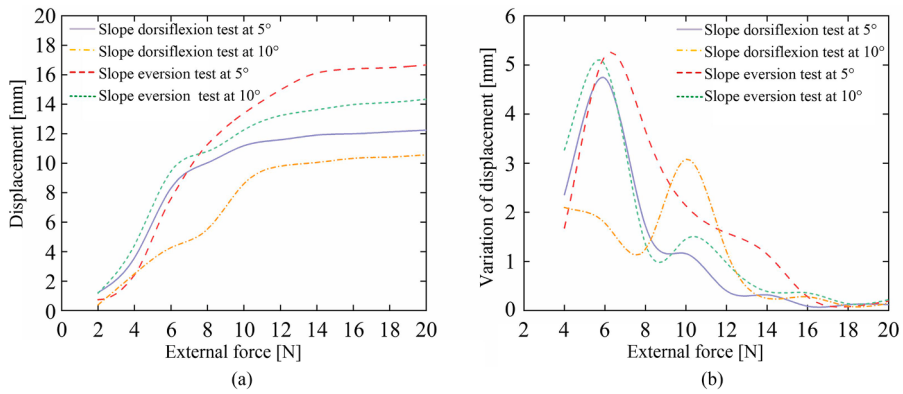


Fig. 17. Variation curve of the experimental results: (a) Displacement curve; (b) Displacement variation curve.

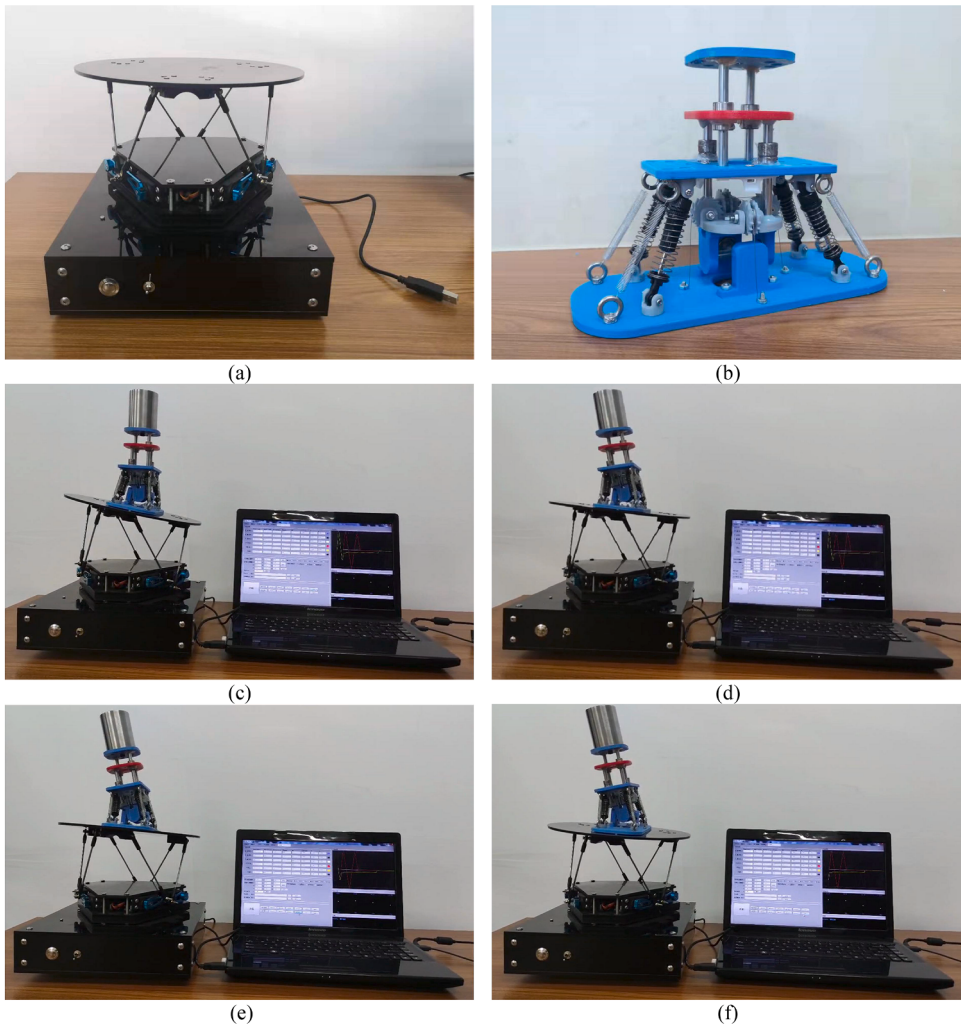


Fig. 18. Test experiment of the locking mechanism performance: (a) 6-degree-of-freedom motion platform; (b) Physical prototype model of the foot structure; (c)~(f) Stability test experiment of the foot structure under a locking condition after being loaded.

$$\theta = \frac{\Delta L_1}{r} \quad (31)$$

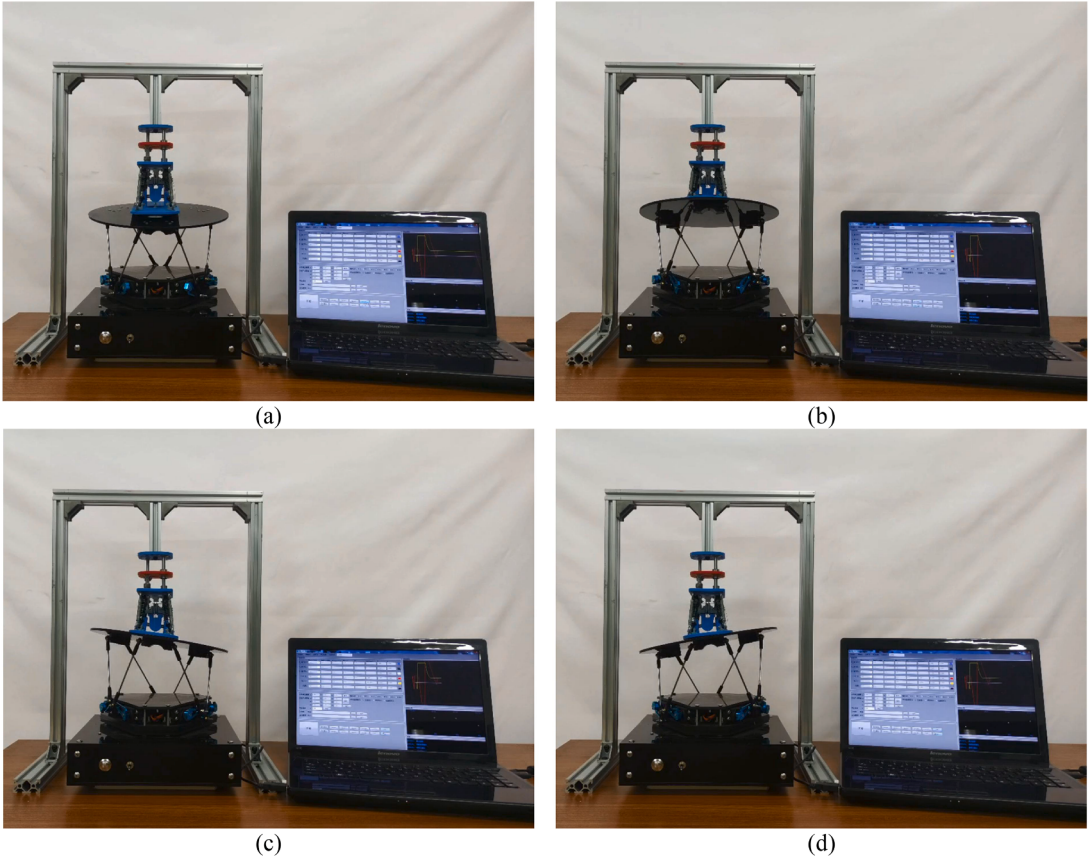


Fig. 19. Adaptive performance tests: (a) The plantar flexion motion of the foot structure; (b) The dorsiflexion motion of the foot structure; (c) The valgus motion of the foot structure; (d) The inversion motion of the foot structure.

where $\Delta L_1 = L_1 - L_1^0$. In the current state $L_3^0 - \Delta L_1 > L_3$, i.e., when θ is the clockwise deflection angle of bar 13, the cable connected to ratchet gear *B* at node *A* is in tension, and the cable connected to ratchet gear *C* at node *E* is in slack.

Then, when bar 13 is deflected clockwise, the relationship between the deflection angle γ and the ratchet rotation angle θ can be expressed as

$$\theta = \frac{\sqrt{[L_{OA} - L_S \cos(\gamma + 60^\circ)]^2 + [L_h + L_S \sin(\gamma + 60^\circ)]^2 - r^2} - \sqrt{(L_{OA} - \frac{L_S}{2})^2 + (\frac{\sqrt{3}}{2}L_S - L_h)^2}}{r} \quad (32)$$

4. Experiments

4.1. Stability tests

To verify the stability of the new foot structure based on the MOTS, a physical prototype of the foot structure was fabricated based on the theory described above, as shown in Fig. 15(b).

The new foot structure based on the MOTS discussed in this paper is a passive type of foot structure; Thus, the initial state is a spatially symmetric stable form when not subjected to external loading. Throughout the walking process, the human foot will adapt to the terrain, and when the foot is in stable contact with the ground, the foot will be subject to its own gravity. To further test the prototype and simulate the situation where the human foot is loaded and can remain in a stable state during walking, a vertical push-pull test rig was used to conduct experiments on the structure.

The test platform is set up with 5° and 10° slopes to simulate different terrains. The experimental platform is shown in Fig. 16(a). The upper end of the prototype is fixed with a push-pull meter, the bottom surface of the prototype is suspended above the slope, and the bottom surface is not in contact with the slope. The digital display push-pull meter and the digital display scale in this position are zeroed, and this state is taken as the initial position. Pressure is applied on the prototype by varying the displacement downward and gradually increasing the load force in steps of 2 N. Changes in the prototype and the digital display push-pull meter are observed, and the displacement shown by the digital display scale is recorded. In Figs. 16(b) to (e), the image sequence shows the process of stress

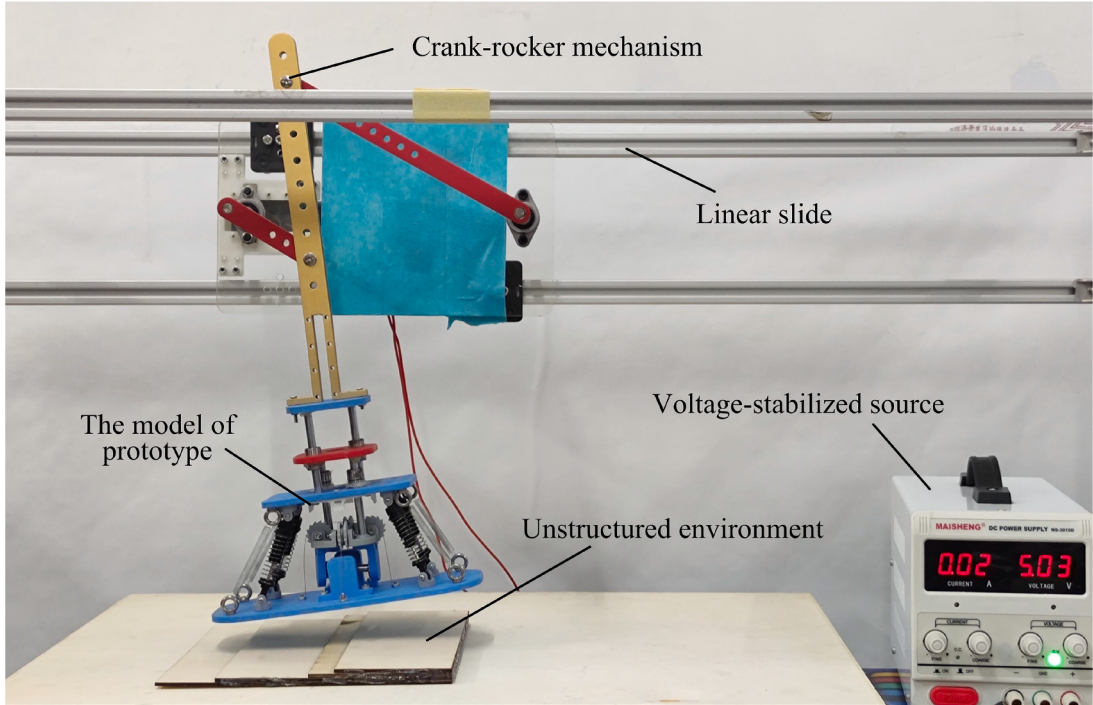


Fig. 20. Foot structure simulation walking experiment platform.

testing the prototype.

From Figs. 16(b) to (e), the foot structure gradually transitions from the adapted slope state (Figs. 16(b) and 16(c)) to the locked state (Figs. 16(d) and 16(e)) under gradual pressure loading. The dorsiflexion and eversion state displacement data from the digital display for the foot structure on the 5° slope and 10° slope under the external load are shown in Table 2. The displacement curve (Fig. 17(a)) and displacement variation curve (Fig. 17(b)) of the experimental results show that with increasing load force, the displacement of the prototype gradually leveled off, and the variation of the prototype displacement gradually decreased and stabilized. Fig. 17(b) shows that when the load force exceeds 14 N, the foot structure switches to the locked state, and in the locked state, the foot structure can withstand the external load within a certain range. (As shown in Table 2 and Fig. 17, when the load force is less than 14N, because of the moving vice that exists in the vertical direction of the foot structure, a large displacement deformation occurs during the applied load as the bottom adaptive terrain changes. When the load force exceeds 14N, the foot structure reaches the locked state and the prototype will not deform displacement in theory. However, due to the effect of the elastic deformation of the prototype material, a small deformation is generated during the applied load.)

4.2. Foot structure locking mechanism performance and self-adaptability tests

The locking mechanism works on the principle that after the foot structure adapts itself to the deformation of the slope, the rotation of the ratchet will lock when subjected to a load to thus realize the state of the rigid foot structure from the flexible adaptive road surface to the rigid foot structure. To verify the performance of the locking mechanism for the foot structure, a 1-kg weight is used to simulate the load applied on the foot structure. Before the experiment begins, the 6-degree-of-freedom motion platform is first adjusted to the state shown in Fig. 18(a), and the experiment is conducted in the inversion state of the foot structure. In addition, the 6-degree-of-freedom motion platform is controlled to move after the load is applied. Morphological changes in the foot structure were observed. The experimental results show that the foot structure does not undergo morphological changes when subjected to a locked state of load. The stability testing process of the foot structure under locking conditions after being loaded is shown in Figs. 18(c)~(f).

To test the adaptive motion performance of the foot structure, a test bench was built using a 6-degree-of-freedom planar motion platform, as shown in Fig. 19. The upper end of the foot structure is fixed according to the stability of the human center of gravity, the sole foot is in contact with the plane of the 6-degree-of-freedom motion platform, and the plane motion of the 6-degree-of-freedom motion platform is controlled by a computer during the test. The experimental results show that the foot structure can adapt well to the planar motion of a 6-degree-of-freedom moving platform.

From the adaptive capacity test of the foot structure, the plantar flexion motion of the foot structure is shown in Fig. 19(a), the dorsiflexion motion is shown in Fig. 19(b), the valgus motion is shown in Fig. 19(c), and the inversion motion is shown in Fig. 19(d). Since the foot structure is built using a theory based on the MOTS, it is mainly composed of continuous elastic members and discontinuous rigid rods with superior flexibility and self-adaptability.

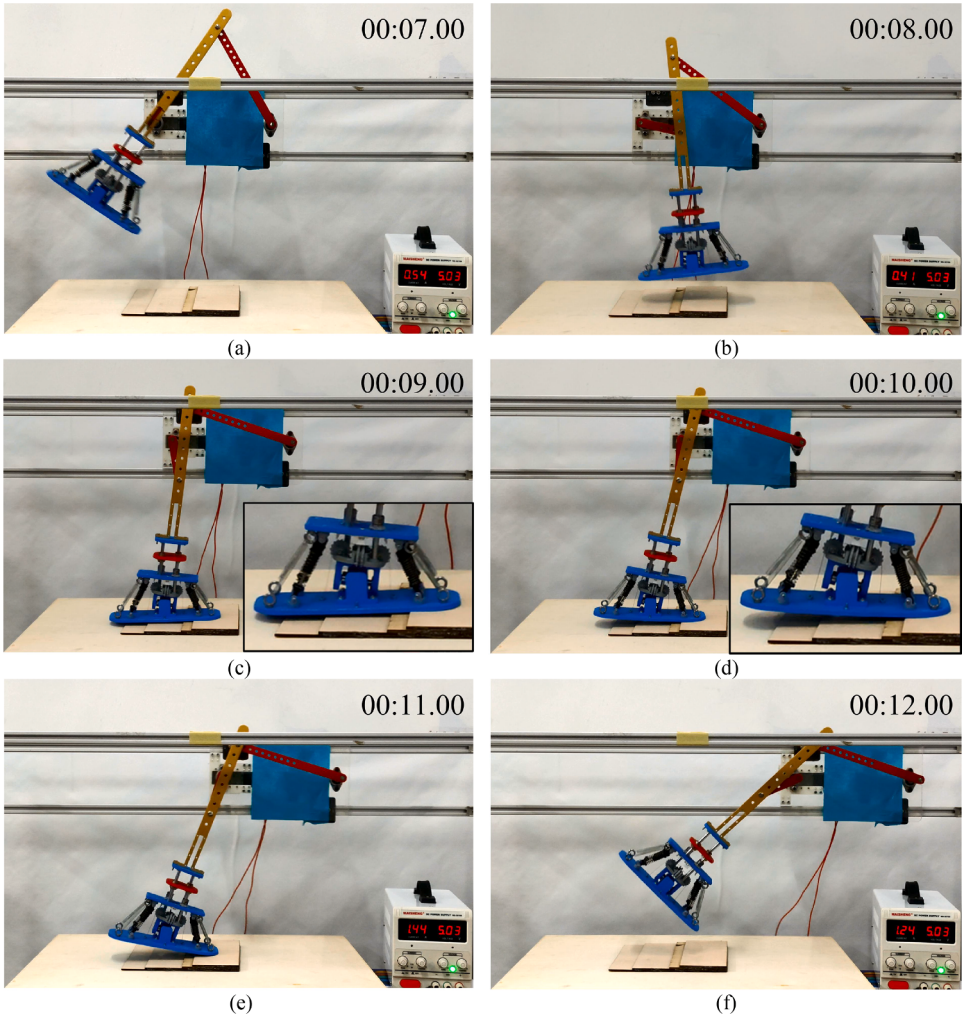


Fig. 21. The walking test experiment: (a)~(f) Simulation of foot movement characteristics during the walking test experiment of the foot structure.

4.3. Foot structure simulation of the movement characteristics during the walking tests

An aluminum profile linear guide is used in the walking experimental platform, as shown in Fig. 20. The platform primarily consists of a linear guide, crank rocker mechanism, and uneven hardwood board. A single-motor driven crank rocker mechanism is used to simulate the motion of the lower leg during walking. The lower end of the output rocker in the crank rocker mechanism is fixed with the foot structure. The motor and crank rocker mechanism can move freely along the profile rail, and the uneven plane of the board is used to simulate an unstructured environment during walking. The test procedure to simulate foot motion characteristics during walking is shown in Figs. 21(a)~(f). The experimental results show that the new foot structure based on the MOTS can better simulate the motion characteristics of the foot during walking.

During the tests shown in Figs. 21(a) to (f), the foot structure produced morphological changes that adapted to the terrain as the foot structure simulated walking on a rough road surface. When leaving the rough road, the foot structure is restored to its initial state with the support of the MOTS. For this work, the experimental results fully demonstrate the good stability, excellent self-adaptive capability and full locking ability of the new foot structure based MOTS.

4.4. Measuring ankle joint angle changes in walking gait cycles

During gait walking, there are four main stages of the foot during a gait cycle: heel-strike, foot-flat, heel-rise, and toe-off. Manual simulation of foot movements during the walking gait cycle. By using the Qualisys-Miqus M3 3D motion capture system for 3D capture analysis of the walking gait, the capture nodes A, B, and C are arranged on the foot structure, as shown in Fig. 22(a). The experimental results of the angle change of the ankle joint during one gait cycle are shown in Fig. 22(b). For comparison, the standard curve of the angle change of the human ankle joint [35] is also shown in Fig. 22(b). The 3D motion capture system was experimental process

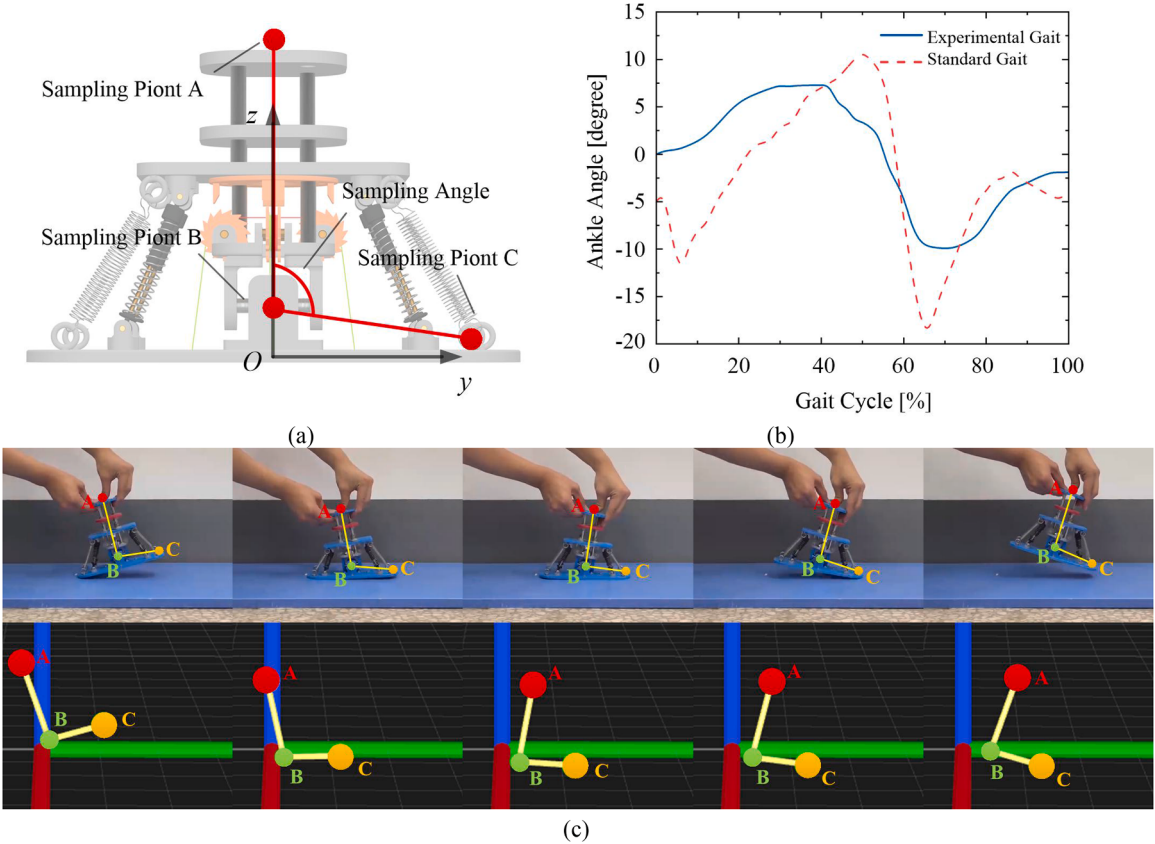


Fig. 22. Measuring ankle joint angle changes in walking gait cycles using a 3D motion capture system:(a) Points A, B and C represent the captured marker positions; (b) The experimental results of variation in ankle joint angle; (c) 3D motion capture system experimental process diagram.

diagram, as shown in Fig. 22(c).

The comparative observation in Fig. 22(b) shows that the tendency of the resultant data curve of the 3D motion capture system is in accordance with the trend of the human ankle joint, and the significant differences that exist are mainly due to the manual experimental simulation. The experimental results show that the ankle joint motion angle of the new foot structure can meet the requirements of the robot foot motion.

5. Conclusion

In this study, a new foot structure based on a mast-type octahedral tensegrity structure was proposed. The main contributions of this work include innovative design, simulation analysis, work space solution, and functional testing, which provide a further horizon of research and development for the foot mechanisms. The main conclusions of this paper are as follows.

- (1) A new tensegrity structure (eMOTS) with the ability to meet the requirements of human foot movement space was proposed by equivalently replacing specific bars in the mast-type octahedral tensegrity structure.
- (2) A new type of foot structure was designed based on the eMOTS structure, featuring two modes of rigid support and flexible adaptation. The foot structure has self-adaptability, self-stability, and self-recovery characteristics in the flexible adaptation mode, which can be employed to improve adaptability when walking through passive deformation. The foot structure switches to a rigid structure in the rigid support mode, which can provide more support for walking. This switching process is spontaneously as the foot structure is subjected to different loads.
- (3) The locking structure based on the ratchet structure realizes the switch between the flexible adaptation state and the rigid support state of the tensioned integral foot structure, which avoids the low structural stability of the tensioned integral foot structure caused by too many degrees of freedom and ensures the stability of the support in the walking process.

The foot structure proposed in this paper is an extended study of the structure in the literature [31]. Comparison with the structure in literature [31], the new type foot structure based on the eMOTS has fewer types of elastic members, and it is easier in the process of stiffness matching. It featured two stable states to ensure the stability of the support during walking.

This research is limited to verify walking performance and lack of partial theoretical modeling. In the follow-up work, we will add a metatarsophalangeal joint to the foot structure that has the characteristic of tensegrity structure and use the flexion and extension characteristics of the toe structure to improve the smoothness of the human running and walking process, thus ensuring the smoothness of the metatarsal gait and the pressure stability of the toe gait, and providing a unified solution for both walking and running.

Declaration of Competing Interest

The authors declare that they have no known competing financial interests or personal relationships that could have appeared to influence the work reported in this paper.

Acknowledgements

This project was supported by the National Natural Science Foundation of China [No. 51775054] and the Jilin Scientific and Technological Development Program [No. 20210509041RQ]. All findings and results presented in this paper are those of the authors and do not represent those of the funding agencies. We wish to thank American Journal Experts (AJE) for their indispensable assistance in the editing of this paper.

Supplementary materials

Supplementary material associated with this article can be found, in the online version, at doi:[10.1016/j.mechmachtheory.2022.105016](https://doi.org/10.1016/j.mechmachtheory.2022.105016).

References

- [1] R. Versluys, P. Beyl, M. Van Damme, A. Desomer, R. Van Ham, D. Lefeber, Prosthetic feet: State-of-the-art review and the importance of mimicking human ankle-foot biomechanics, *Disabil. Rehabil. Assist. Technol.* 4 (2009) 65–75, <https://doi.org/10.1080/17483100802715092>.
- [2] B.J. Hafner, J.E. Sanders, J. Czerniecki, J. Fergason, Energy storage and return prostheses: does patient perception correlate with biomechanical analysis? *Clin. Biomech.* 17 (2002) 325–344, [https://doi.org/10.1016/S0268-0033\(02\)00020-7](https://doi.org/10.1016/S0268-0033(02)00020-7).
- [3] D. Kim, S.J. Jorgensen, J. Lee, J. Ahn, J. Luo, L. Sentis, Dynamic locomotion for passive-ankle biped robots and humanoids using whole-body locomotion control, *Int. J. Robot. Res.* 39 (8) (2020) 936–956, <https://doi.org/10.1177/0278364920918014>.
- [4] H. Xiu, Y. Han, X. Wang, Y. Zhang, W. Liang, G. Wei, L. Ren, L. Ren, Design, development, and clinical validation of a two degrees of freedom compliant ankle-foot prosthesis based on a 4-4r parallel mechanism, *Mech. Mach. Theory* 172 (2022), 104818, <https://doi.org/10.1016/j.mechmachtheory.2022.104818>.
- [5] M.K. Shepherd, E.J. Rouse, The VSPA foot: A quasi-passive ankle-foot prosthesis with continuously variable stiffness, *IEEE Trans. Neural Syst. Rehabil. Eng.* 25 (2017) 2375–2386, <https://doi.org/10.1109/TNSRE.2017.2750113>.
- [6] E. Nickel, J. Sensinger, A. Hansen, Passive prosthetic ankle-foot mechanism for automatic adaptation to sloped surfaces, *J. Rehabil. Res. Dev.* 51 (2014) 803–814, <https://doi.org/10.1682/JRRD.2013.08.0177>.
- [7] J. Realmuto, G. Klute, S. Devasia, Nonlinear passive cam-based springs for powered ankle prostheses, *J. Med. Devices, Trans. ASME*. (2015) 9, <https://doi.org/10.1115/1.4028653>.
- [8] J.D. Lee, L.M. Mooney, E.J. Rouse, Design and characterization of a quasi-passive pneumatic foot-ankle prosthesis, *IEEE T Neur. Sys. Reh.* 25 (2017) 823–831, <https://doi.org/10.1109/TNSRE.2017.2699867>.
- [9] Y.L. Park, B.C. Chen, N. Pérez-Arcibia, D. Young, L. Stirling, R.J. Wood, E.C. Goldfield, R. Nagpal, Design and control of a bio-inspired soft wearable robotic device for ankle-foot rehabilitation, *Bioinspir. Biomim.* 9 (2014), 016007, <https://doi.org/10.1088/1748-3182/9/1/016007>.
- [10] B. Chen, B. Zi, Z.Y. Wang, Y. Li, J. Qian, Development of robotic ankle-foot orthosis with series elastic actuator and magneto-rheological brake, *J. Mech. Robot.* (2021) 13, <https://doi.org/10.1115/1.4047987>.
- [11] K.X. Ba, B. Yu, G.L. Ma, Z.J. Gao, Q.X. Zhu, Z.G. Jin, X.D. Kong, Dynamic compliance analysis for LHDS of legged robot, part a: position-based impedance control, *IEEE Access* 6 (2018) 64321–64332, <https://doi.org/10.1109/ACCESS.2018.2875121>.
- [12] Z. Issabekov, N. Aldiyarov, Developing the mathematical model of the bipedal walking robot executive mechanism, *Int. J. Adv. Comput. Sci.* 12 (2021) 304–308, <https://doi.org/10.14569/IJACSA.2021.0121240>.
- [13] F. Sup, A. Bohara, M. Goldfarb, Design and control of a powered transfemoral prosthesis, *Int. J. Rob. Res.* 27 (2008) 263–273, <https://doi.org/10.1177/0278364907084588>.
- [14] S.K. Au, H. Herr, J. Weber, E.C. Martinez-Villalpando, Powered ankle-foot prosthesis for the improvement of amputee ambulation, *Annu. in: 2007 29th Int. Conf. IEEE Eng. Med. Biol.* 2007–August, 2007, pp. 3020–3026, <https://doi.org/10.1109/EMBS.2007.4352965>.
- [15] J. Pransky, The Pransky interview: Dr. Hugh Herr – Professor, MIT media lab; director, Biomechatronics Group and Co-director, MIT center for extreme bionics; founder, BionX Medical Technologies Inc., *Ind. Rob.* 47 (2020) 795–799, <https://doi.org/10.1108/IR-06-2020-0115>.
- [16] P. Cherelle, V. Grosu, A. Matthys, B. Vanderborght, D. Lefeber, Design and validation of the ankle mimicking prosthetic (AMP-) Foot 2.0, *IEEE Trans. Neural Syst. Rehabil. Eng.* 22 (2014) 138–148, <https://doi.org/10.1109/TNSRE.2013.2282416>.
- [17] Y. Feng, Q. Wang, Combining push-off power and nonlinear damping behaviors for a lightweight motor-driven transtibial prosthesis, *IEEE/ASME Trans. Mechatronics*. 22 (2017) 2512–2523, <https://doi.org/10.1109/TMECH.2017.2766205>.
- [18] D. Dong, W. Ge, S. Liu, F. Xia, Y. Sun, Design and optimization of a powered ankle-foot prosthesis using a geared five-bar spring mechanism, *Int. J. Adv. Robot. Syst.* 14 (2017) 1–12, <https://doi.org/10.1177/1729881417704545>.
- [19] T. Lenzi, M. Cempini, L.J. Hargrove, T.A. Kuiken, Design, Development, and validation of a lightweight nonbackdrivable robotic ankle prosthesis, *IEEE/ASME Trans. Mechatronics*. 24 (2019) 471–482, <https://doi.org/10.1109/TMECH.2019.2892609>.
- [20] Y. Liu, Q. Bi, X. Yue, J. Wu, B. Yang, Y. Li, A review on tensegrity structures-based robots, *Mech. Mach. Theory* 168 (2022), 104571, <https://doi.org/10.1016/j.mechmachtheory.2021.104571>.
- [21] A.P. Sabelhaus, H. Ji, P. Hylton, Y. Madaan, C.W. Yang, A.M. Agogino, J. Friesen, V.S. Spiral, Mechanism design and simulation of the ultra spine, a tensegrity robot, *ASME Des. Eng. Tech. Conf.* (2015) 1–12, <https://doi.org/10.1115/DETC2015-47583>.
- [22] J. Rieffel, J.B. Mouret, Adaptive and resilient soft tensegrity robots, *Soft Robot* 5 (2018) 318–329, <https://doi.org/10.1089/soro.2017.0066>.

- [23] B.T. Mirletz, P. Bhandal, R.D. Adams, A.K. Agogino, R.D. Quinn, V.S. Spiral, Goal-directed CPG-based control for tensegrity spines with many degrees of freedom traversing irregular terrain, *Soft Robot* 2 (2015) 165–176, <https://doi.org/10.1089/soro.2015.0012>.
- [24] J. Cui, P. Wang, T. Sun, S. Ma, S. Liu, R. Kang, F. Guo, Design and experiments of a novel quadruped robot with tensegrity legs, *Mech. Mach. Theory* 171 (2022), 104781, <https://doi.org/10.1016/j.mechmachtheory.2022.104781>.
- [25] G. Scarr, A consideration of the elbow as a tensegrity structure, *Int J Osteopath Med* 15 (2012) 53–65, <https://doi.org/10.1016/j.ijosm.2011.11.003>.
- [26] W.Y. Li, H. Nabae, G. Endo, K. Suzumori, New soft robot hand configuration with combined biotensegrity and thin artificial muscle, *IEEE Robot. Autom. Lett* 5 (2020) 4345–4351, <https://doi.org/10.1109/LRA.2020.2983668>.
- [27] L.B. Baltaxe-Admony, A.S. Robbins, E.A. Jung, S. Lessard, M. Teodorescu, V. SunSpiral, A. Agogino, Simulating the human shoulder through active tensegrity structures, *ASME Des. Eng. Tech. Conf.* 6 (2016) 1–6, <https://doi.org/10.1115/DETC2016-60157>.
- [28] J. Sun, X. Cao, G. Song, Design method for a bionic wrist based on tensegrity structures, *Biosurface and Biotribology* 6 (2020) 31–36, <https://doi.org/10.1049/bsbt.2019.0022>.
- [29] E. Jung, V. Ly, A. Buderer, E. Appleton, M. Teodorescu, Design and selection of muscle excitation patterns for modeling a lower extremity joint inspired tensegrity, *Proceedings of the Third IEEE International Conference on Robotic Computing (IRC)* (2019) 282–287, <https://doi.org/10.1109/IRC.2019.00053>.
- [30] G. Lee, G.Y. Hong, Y. Choi, Tendon-driven compliant prosthetic wrist consisting of three rows based on the concept of tensegrity structure, *IEEE Robot. Autom. Lett.* 6 (2021) 3956–3963, <https://doi.org/10.1109/LRA.2021.3067237>.
- [31] J. Sun, G. Song, J. Chu, L. Ren, An adaptive bioinspired foot mechanism based on tensegrity structures, *Soft Robot.* 6 (2019) 778–789, <https://doi.org/10.1089/soro.2018.0168>.
- [32] R.E. Skelton, M.C. De Oliveira, *Tensegrity Systems*, Springer, Boston, MA, 2009, <https://doi.org/10.1007/978-0-387-74242-7>.
- [33] C. Sultan, M. Corless, R.E. Skelton, Linear dynamics of tensegrity structures, *Eng. Struct.* 24 (2002) 671–685, [https://doi.org/10.1016/S0141-0296\(01\)00130-4](https://doi.org/10.1016/S0141-0296(01)00130-4).
- [34] G.G. Estrada, H.J. Bungartz, C. Mohrdeick, Numerical form-finding of tensegrity structures, *Int. J. Solids Struct.* 43 (2006) 6855–6868, <https://doi.org/10.1016/j.ijsolstr.2006.02.012>.
- [35] A. Agboola-dobson, Biologically inspired design and development of a variable stiffness powered ankle-foot prosthesis, *J. Mech. Robot.* 11 (2019) 1–15, <https://doi.org/10.1115/1.4043603>.